A Two-Way Nested Global-Regional Dynamical Core on the Cubed-Sphere Grid

LUCAS M. HARRIS*

Program in Atmospheric and Oceanic Sciences, Princeton University, Princeton, New Jersey

SHIAN-JIANN LIN

NOAA/Geophysical Fluid Dynamics Laboratory, Princeton University, Princeton, New Jersey

(Manuscript received 15 August 2011, in final form 15 May 2012)

ABSTRACT

A nested-grid model is constructed using the Geophysical Fluid Dynamics Laboratory finite-volume dynamical core on the cubed sphere. The use of a global grid avoids the need for externally imposed lateral boundary conditions, and the use of the same governing equations and discretization on the global and regional domains prevents inconsistencies that may arise when these differ between grids. A simple interpolated nested-grid boundary condition is used, and two-way updates use a finite-volume averaging method. Mass conservation is achieved in two-way nesting by simply not updating the mass field.

Despite the simplicity of the nesting methodology, the distortion of the large-scale flow by the nested grid is such that the increase in global error norms is a factor of 2 or less in shallow-water test cases. The effect of a nested grid in the tropics on the zonal means and eddy statistics of an idealized Held–Suarez climate integration is minor, and artifacts due to the nested grid are comparable to those at the edges of the cubed-sphere grid and decrease with increasing resolution. The baroclinic wave train in a Jablonowski–Williamson test case was preserved in a nested-grid simulation while finescale features were represented with greater detail in the nested-grid region. The authors also found that lee vortices could propagate out of the nested region and onto a coarse grid, which by itself could not produce vortices. Finally, the authors discuss how concurrent integration of the nested and coarse grids can be significantly more efficient than when integrating the two grids sequentially.

1. Introduction

Global models have many advantages for climate simulation and medium-range weather prediction. Global models do not need externally imposed lateral boundary conditions (BCs), and so there are no issues with boundary errors contaminating the solution, nor inconsistency between the model dynamics and that of the imposed BCs, two major problems for limited-area models (Warner et al. 1997). Global models also allow synoptic- and planetary-scale features to be better represented and to interact with any smaller-scale features that may be resolved by the model. This scale interaction is particularly important for studies of orographic drag and deep convection on the general circulation, and in forecasting hurricanes and other phenomena that feed back onto their large-scale environment.

However, running a global model with uniform grid spacing at scales needed to fully resolve these features is still impractical using today's computers. Regional climate models (RCMs; Giorgi and Mearns 1999) typically require years- or decades-long simulations resolving phenomena only dozens of kilometers wide, and accurate hurricane intensity forecasting may require resolving features only a few kilometers wide.

A better solution would be to use a global model with a locally refined grid, which would represent the large scales globally, use the higher resolution only over the area of interest, and allow the two scales to interact. While any grid refinement will cause errors as disturbances propagate through the refined region, we expect that having the refined and coarse regions in the same

* Current affiliation: NOAA/Geophysical Fluid Dynamics Laboratory, Princeton University, Princeton, New Jersey.

Corresponding author address: Lucas Harris, NOAA/Geophysical Fluid Dynamics Laboratory, Princeton University, Forrestal Campus, 201 Forrestal Road, Princeton, NJ 08540-6649.
E-mail: lucas.harris@noaa.gov

DOI: 10.1175/MWR-D-11-00201.1

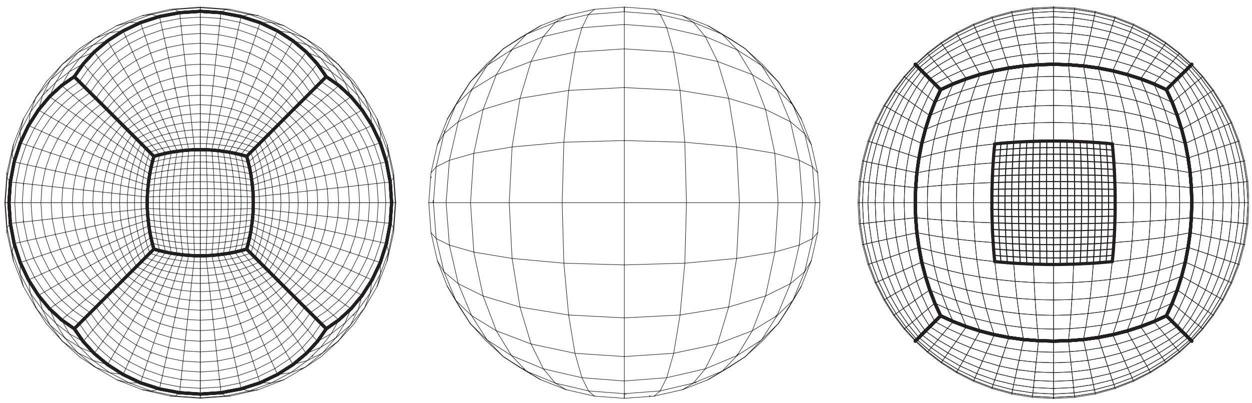

FIG. 1. Methods for locally refining a global grid. (left) A stretched cubed-sphere grid, whose smallest face has been scaled by a factor of 3 in both directions. (middle) Reverse of stretched grid showing coarsest face, which covers more than half the sphere. (right) A nested grid in an unstretched grid; the nest is a 3:1 refinement of the coarse grid. Thin lines represent local coordinate lines; heavy lines represent cube edges and nested-grid boundaries.

model (complete with the same dynamics and discretization), and having the large-scale data continually supplied to the refined region, would yield smaller boundary errors than if a regional model were to be forced with boundary data from an independent, noninteracting global model. An approach often used in global models is to use a stretched or deformed grid, in which a uniform-resolution grid is transformed so there are more grid points or cells over the region of interest. On the opposite side of the globe there are fewer grid cells and thereby lower resolution, as depicted in Fig. 1, left and middle panels. This capability already exists in several models, including that described in this paper; see Courtier and Geleyn (1988) and Fox-Rabinovitz et al. (2006) for other examples. However, if the stretching is so large that the grid size varies significantly, new problems can occur. The time step of the entire grid will be controlled by the smallest grid spacing in the refined region, which increases the computational expense of the simulation. Furthermore, since physical parameterizations are often scale dependent, unless special parameterizations that adapt to the grid spacing are used, they may only be appropriate for certain parts of the model domain. Finally, the resolution on the side opposite to the refined region may be so much more coarse than in the rest of the domain that disturbances passing through this region may no longer be well-enough resolved to be represented accurately. The resulting errors can propagate into the refined region if the simulation is long enough.

A much less common approach for refining a global model (but very common in limited-area modeling) is to use a two-way nested model (Fig. 1, right), with the global domain acting as the coarse, ''parent'' grid and a regional domain acting as the nested grid, with nested-grid BCs periodically applied from the global grid. Both grids use the same model dynamics and discretization, so the only inconsistency arises from the different resolutions of the two grids. Applying different time steps and physical parameterizations between the two grids is trivial, and the coarse grid domain need not be altered to allow nesting; in particular grid nesting does not require a decrease in global model resolution anywhere, and nests can be placed at an arbitrary number of locations on the globe, or even within one another. Two-way nesting allows for the nested grid to influence the global grid by periodically ''updating'' or replacing the global solution by the nested-grid solution where the grids coincide. Nested grids are also more versatile than stretched grids, as any number of nested grids can be used, grids can be nested within one another, and nests can be rectangular instead of square. Drawbacks of two-way nesting are that the grid boundary is a discontinuous refinement and creates more localized errors than does a gradual refinement (Vichnevetsky 1987; Long and Thuburn 2011, and references therein), and that interaction between the refined and coarse regions only occurs at defined intervals (although typically more frequently than the externally imposed BCs for limited-area models), while for a stretched grid this interaction occurs naturally at every time step.

The authors are aware of a few studies using two-way global-to-regional nested models. Lorenz and Jacob (2005) nested a regional gridpoint model in a spectral global model for a 10-yr climate integration, in order to better represent the topography of the Maritime Continent. Their results were promising—a global decrease in zonally averaged temperature biases was observed in the nested model compared to the single-grid global model—but no further results were shown and no further research using this model appears to exist. Inatsu and

Kimoto (2009) found a result similar to, but less compelling than, that of Lorenz and Jacob (2005), using a similar nesting methodology with a nest over northeast Asia. Chen et al. (2011) used a two-way nested RCM that placed a nest over eastern China, using the same gridpoint model for both the global and nested grids. They found a local reduction in temperature bias, but did not examine the effect of two-way nesting outside of the nested region.

Dudhia and Bresch (2002) presented a test of global-to-regional two-way nesting using the global version of the fifth-generation Pennsylvania State University–National Center for Atmospheric Research (PSU–NCAR) Mesoscale Model (MM5) for a 3-day weather forecast for North America. The 40-km grid-spacing nested grid was able to resolve features that the 120-km grid-spacing global domain could not, with an apparent minimum of distortion at the nested-grid boundary. Similar capability exists in the Weather Research and Forecasting Model (WRF) (Richardson et al. 2007). Transport Model 5 (TM5) (Krol et al. 2005) and the Goddard Earth Observing System–Chemistry model (GEOS-Chem; Bey et al. 2001) are both "offline" chemistry and transport models that can use two-way global-to-regional nesting, but are not dynamical models and rely on reanalysis data or model output from other sources to operate.

In this paper we present a two-way nested idealized model using the Geophysical Fluid Dynamics Laboratory finite-volume (FV) dynamical core (Lin 2004, hereafter L04), discretized on the cubed-sphere geometry of Putman and Lin (2007, hereafter PL07). This dynamical core, henceforth the "FV core," has been very successful in a number of applications, including climate simulation (Delworth et al. 2006; Zhao et al. 2009; Donner et al. 2011), weather prediction (Lin et al. 2004; Atlas et al. 2005), and seasonal hurricane prediction (Chen and Lin, 2011). Both the nested and coarse grids use the same FV core so as to avoid errors that might arise as a result of the use of different solvers on each grid. Any of a number of schemes for the grid coupling can be used in our nested-grid model, although we will show that favorable results can be attained using simple, standard methods, including a straightforward method for conserving mass on the global coarse grid.

The model will be tested using several common idealized test cases. First, a series of standard shallow-water test cases are performed to determine the impact of the nested grid on the large-scale flows that characterize these test cases. The first three-dimensional test case is the baroclinic instability test case of Jablonowski and Williamson (2006), which tests the ability of the nesting to permit individual disturbances to pass into and out of the nested-grid region and to yield a reasonable solution on time scales of one to two weeks. Another is the idealized climate integration of Held and Suarez (1994) that tests the ability of the nested model to preserve the climatology produced during a multiple-year integration. A final test uses real topography and analyzed initial conditions to demonstrate vortices shed in the lee of the Big Island of Hawaii that are able to propagate onto a coarse grid, which could not itself resolve the processes generating the vortices. We also present a comparison of the efficiency of the nested-grid model to uniform-resolution simulations.

Section 2 describes the FV core, cubed-sphere grid geometry, and the nesting methodology. Section 3 describes the results from the test cases. Section 4 concludes the paper.

2. The nested-grid model

a. Finite-volume dynamical core and cubed-sphere grid

The FV core is a hydrostatic, 3D dynamical core using the vertically Lagrangian discretization of L04 and the horizontal discretization of Lin and Rood (1996, 1997, hereafter LR96 and LR97, respectively), using the cubed-sphere geometry of PL07 and Putman (2007). This solver discretizes a hydrostatic atmosphere into a number of vertical layers, each of which is then integrated by treating the pressure thickness and potential temperature as scalars. Each layer is advanced independently, except that the pressure gradient force is computed using the geopotential and the pressure at the interface of each layer (Lin 1997). The interface geopotential is the cumulative sum of the thickness of each underlying layer, counted from the surface elevation upward, and the interface pressure is the cumulative sum of the pressure thickness of each overlying layer, counted from the constant-pressure top of the model domain downward. Vertical transport occurs implicitly from horizontal transport along Lagrangian surfaces. The layers are allowed to deform freely during the horizontal integration. To prevent the layers from becoming infinitesimally thin, and to vertically redistribute mass, momentum, and energy, the layers are periodically remapped to a predefined Eulerian coordinate system.

The governing equations in each horizontal layer are the vector-invariant equations:

$$\frac{\partial \delta p}{\partial t} + \nabla \cdot (\mathbf{V}\delta p) = 0,$$

$$\frac{\partial \delta p\Theta}{\partial t} + \nabla \cdot (\mathbf{V}\delta p\Theta) = 0,$$

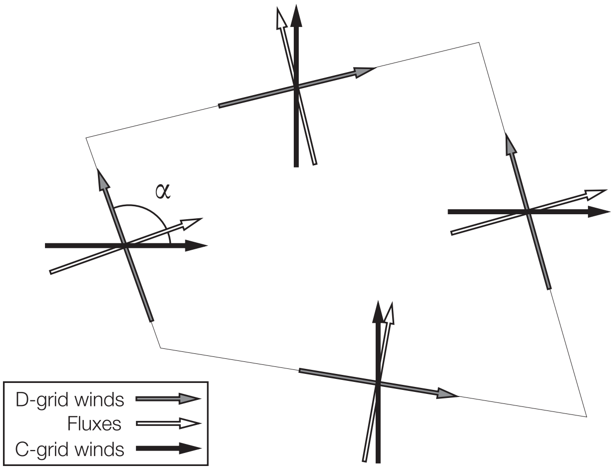

FIG. 2. Geometry of the wind staggerings and fluxes for a cell on a nonorthogonal grid. The angle α is that between the covariant and contravariant components; in orthogonal coordinates $\alpha = \pi/2$.

$$\frac{\partial \mathbf{V}}{\partial t} = -\Omega \hat{\mathbf{k}} \times \mathbf{V} - \nabla(\kappa + \nu \nabla^2 D) - \frac{1}{\rho} \nabla p \bigg|_z ,$$

where the prognostic variables are the hydrostatic pressure thickness δp of a layer bounded by two adjacent Lagrangian surfaces, which is proportional to the mass of the layer; the potential temperature Θ; and the vector wind $\mathbf{V}$. Here, $\hat{\mathbf{k}}$ is the vertical unit vector. The other variables are diagnosed: the density ρ, kinetic energy $\kappa = (1/2)\|\mathbf{V}\|$, divergence D, pressure p, and absolute vertical vorticity Ω. Finally, the prescribed higher-order ∇^4 divergence damping strength is given by ν.

We use the gnomonic coordinate of PL07, in which coordinate lines are great circles, to define our horizontal discretization. This coordinate yields more uniformly sized cells over the whole sphere, but is nonorthogonal. As a result, the prognosed covariant wind components u and v differ from the diagnosed contravariant wind components $\tilde{u}$ and $\tilde{v}$ that are required for the transport operator. Define $\mathbf{V} = \tilde{u}\mathbf{e}_x + \tilde{v}\mathbf{e}_y$, where $\mathbf{e}_x$ and $\mathbf{e}_y$ are the local unit vectors of the coordinate system. The covariant components of the wind are then $u = \mathbf{V} \cdot \mathbf{e}_x$ and $v = \mathbf{V} \cdot \mathbf{e}_y$, and the kinetic energy is $\kappa = (1/2)(u\tilde{u} + v\tilde{v})$. The angle α between the local unit vectors is given by $\sin\alpha = \|\mathbf{e}_x \times \mathbf{e}_y\|$; in an orthogonal coordinate system, $\alpha = \pi/2$.

The horizontal discretization is derived using a finite-volume integration about a 2D quadrilateral grid cell with area ΔA and over a time step of length $\Delta\tau$, with the winds staggered on a D grid (Fig. 2). The discretized equations are as in Putman (2007), modified for a nonorthogonal coordinate system:

$$\delta p^{n+1} = \delta p^n + F[\widetilde{u^*}, \Delta\tau, \delta p^y] + G[\widetilde{v^*}, \Delta\tau, \delta p^x], \quad (1)$$

$$\Theta^{n+1} = \frac{1}{\delta p^{n+1}} \{\Theta^n \delta p^n + F[x^*, \Delta\tau, \Theta^y] + G[y^*, \Delta\tau, \Theta^x]\}, \quad (2)$$

$$u^{n+1} = u^n + \Delta\tau[Y(\widetilde{v^*}, \Delta\tau, \Omega^x) - \delta_x(\kappa^* - \nu\nabla^2 D) + \widehat{P}_x], \quad (3)$$

$$v^{n+1} = v^n + \Delta\tau[X(\widetilde{u^*}, \Delta\tau, \Omega^y) - \delta_y(\kappa^* - \nu\nabla^2 D) + \widehat{P}_y]. \quad (4)$$

In these equations and for the remainder of the article δp, Θ, and other scalar variables are understood as cell-averaged values, and winds and fluxes as face-averaged values. The superscript n represents the time level of the prognostic variables. The flux operators F, G, X, and Y use the contravariant C-grid winds $\widetilde{u^*}$ and $\widetilde{v^*}$, defined at the $n + 1/2$ time level; for Θ the airmass fluxes $x^* = X(\widetilde{u^*}, \Delta\tau, \delta p)$ and $y^* = Y(\widetilde{v^*}, \Delta\tau, \delta p)$ are used. Airmass fluxes would also be used for any tracer species, although we do not use any in the simulations in this paper. The difference operator is defined as $\delta_x \eta = \eta[x + (\Delta x/2)] - \eta[x - (\Delta x/2)]$, and similarly for δ_y.

The fluxes through a cell face are denoted $X(\widetilde{u^*}, \Delta\tau, \eta)$ and $Y(\widetilde{v^*}, \Delta\tau, \eta)$ for an arbitrary scalar η. The fluxes are computed using the piecewise-parabolic method (PPM; Colella and Woodward 1984) using the monotonicity constraint of L04. The use of a monotonicity constraint not only eliminates unphysical overshoots in the solution, but also acts as a diffusive filter that is more physically consistent than ad hoc scale-selective Laplacian diffusion or hyperdiffusion operators. For the Williamson case-2 and -5 shallow-water tests described in sections 3a(1) and 3a(2), we use the modified Suresh and Huynh (1997) scheme described in PL07 without a monotonicity constraint to facilitate comparison to other numerical schemes that typically present convergence tests performed without shape preservation.

The flux divergences (referred to as "outer operators" in PL07 and LR96) in each coordinate direction are

$$F[\widetilde{u^*}, \Delta\tau, \eta] = -\frac{\Delta\tau}{\Delta A} \delta_x [X(\widetilde{u^*}, \Delta\tau, \eta) \Delta y \sin\alpha]$$

$$G[\widetilde{v^*}, \Delta\tau, \eta] = -\frac{\Delta\tau}{\Delta A} \delta_y [Y(\widetilde{v^*}, \Delta\tau, \eta) \Delta x \sin\alpha]$$

for cell face lengths Δx, Δy, so that $\Delta x \sin\alpha$ is the length of a cell face in the direction perpendicular to the flux through that face. The angle α is computed locally, on the cell face on which the flux is being computed. The *advective-form* inner operators, denoted by a superscript x or y, are

$$\eta^x = \frac{1}{2}\left\{\eta + \frac{\eta + F[\widetilde{u^*}, \Delta\tau, \eta]}{1 + F[\widetilde{u^*}, \Delta\tau, 1]}\right\}$$

$$\eta^y = \frac{1}{2}\left\{\eta + \frac{\eta + G[\widetilde{v^*}, \Delta\tau, \eta]}{1 + G[\widetilde{v^*}, \Delta\tau, 1]}\right\}.$$

Using the inner operators to produce a scalar field that is then used in the outer operators in (1)–(4) produces a spatially symmetric scheme that cancels the leading-order splitting error (LR96, their section 2). Using advective-form operators for the inner operator does not affect mass conservation, since the outer operators are still flux form, but allows the scheme to preserve an initially uniform mass field in a nondivergent flow and is thus more physically consistent. The denominator of the second term in the inner operators is a divergence-correction term (PL07). For a particular variable, we use the same computation for X and Y in both the inner and outer operators, which avoids a potential instability (Lauritzen 2007) in the absence of a monotonicity constraint.

The transported kinetic energy κ^* is simply $1/2[X(\widetilde{u^*}, \Delta\tau, u) + Y(\widetilde{v^*}, \Delta\tau, v)]$; using this form avoids the Hollingsworth–Kåallberg instability (Hollingsworth et al. 1983; LR97, p. 2481). The finite-volume absolute vorticity and divergence are given by Ω and D, respectively. Finally, the pressure gradient forces $\widehat{P}_x$ and $\widehat{P}_y$ are computed as in Lin (1997), by integrating around a 2D plane in the vertical.

The time stepping (LR97) uses a forward–backward procedure to advance the cell-averaged values and the D-grid winds. First, the half-time-step C-grid winds $\widetilde{u^*}$, $\widetilde{v^*}$ are computed using first-order vorticity and kinetic energy fluxes, and a pressure gradient force computed using mass and potential temperature advanced to the half time step, also using first-order upwind fluxes. The half-time-step mass and potential temperature are then discarded. A similar procedure is performed to advance the D-grid winds, mass, and potential temperature a full time step, using the full PPM fluxes computed with the half-time-step C-grid winds, and again using a pressure gradient force computed with pressure and temperature advanced to the $n + 1$ time level.

In some cases the solution can be improved by relaxing the backward evaluation of the pressure gradient force, and instead using a weighted average of that force evaluated at time levels n and $n + 1$. This is done by setting a parameter β between 0, for which the pressure gradient force is entirely that computed using pressure and temperature at the $n + 1$ time level, and 1, for which the pressure gradient force is entirely that computed using pressure and temperature at the n time level. In the x direction, the weighting would have the following form:

$$\widehat{P}_x = (1 - \beta)\widehat{P}_x^{\,n+1} + \beta\widehat{P}_x^{\,n}. \tag{5}$$

The use of nonzero β reduces the damping of high-frequency gravity waves. Using $\beta = 0.4$ was found to improve some of the simulations in this paper. Unless otherwise noted, in this paper we will use $\beta = 0$.

Nearly any vertically monotonic quantity can be used as the base for the Eulerian coordinate; here, we use a 32-level hybrid σ–p terrain-following vertical coordinate (Chen and Lin 2011; Zhao et al. 2009), in which for given constants a_k, b_k for each layer interface $k = 1, \ldots, N + 1$ and N layers, the pressure at each Eulerian layer interface is $p_k = a_k + b_k p_s$ for surface pressure $p_s = p_{N+1} = p_T + \sum_{k=1}^{N} \delta p_k$ and pressure at the model top $p_T = 100$ Pa; the new δp_k in the kth layer is $p_{k+1} - p_k$. The resulting surface pressure is the same, and so this procedure trivially conserves air mass. The remapping of other variables is done using piecewise-parabolic subgrid reconstructions in the Lagrangian layers, and then analytically integrating these over each Eulerian layer; full details are in L04. The vertical remapping conserves mass and momentum; an option exists to conserve total energy, although it is not used by the simulations in this paper. Instead, vertical remapping is applied to the temperature, a simpler procedure that conserves geopotential. Remapping need not be applied at every dynamical time step, and indeed can be applied once every hour or even less frequently.

b. Grid-nesting methodology

The nested grid is simply a refinement of one of the faces of the gnomonic cubed sphere: for a refinement ratio r each coarse-grid cell is split into r^2 cells by dividing the great-circle arcs bounding each cell into r equal segments. Our nested grids are aligned with the coarse grid, making grid coupling more accurate and less complicated, but this does force the nested grid to remain on one panel of the cubed-sphere grid. Table 1 gives the positions and sizes of the nested grid in each nested simulation performed in this paper.[1]

Many methods exist for nested-to-coarse-grid coupling (cf. Zhang et al. 1986; Warner et al. 1997; Harris and Durran 2010). However, we will show later that our

[1] Table 1 shows the position of the nested grid's "bottom left" corner in each cubed-sphere panel's local coordinate system. Since the coordinate system in each panel is not necessarily the same as in any other panel, the bottom-left corner in a particular coordinate system is not necessarily the true southwest corner.

TABLE 1. Locations and sizes of nested grids. The coarse-grid grid positions of the nested grid's bottom-left corner I_0 and J_0 are defined in the appendix; note that these are in terms of the local coordinate system on the cubed-sphere panel in which the nested grid lies and need not correspond to the ''southwest'' corner of the grid. Latitude is given in °N and longitude is given in °E, both rounded to the nearest tenth of a degree. The abbreviations ''JW'' and ''HS'' stand for the Jablonowski–Williamson and the Held–Suarez test cases, respectively.

Test case	Grid spacing	Corner of nested grid: Lat, lon	Corner of nested grid: (I_0, J_0)	Nest size
Case 2	c24	(15.8°N, 196.4°E)	(9, 9)	24 × 24
	c36		(13, 13)	36 × 36
	c48		(17, 17)	48 × 48
	c60		(21, 21)	60 × 60
	c90		(31, 31)	90 × 90
	c180		(61, 61)	180 × 180
Case 5	c30	(51.7°N, 142.6°E)	(5, 5)	60 × 60
	c60		(9, 9)	120 × 120
	c90		(13, 13)	180 × 180
	c180		(25, 25)	360 × 360
Case 6	c48	(15.8°N, 196.4°E)	(17, 17)	48 × 48
	c180		(61, 61)	180 × 180
JW	c60	(32.2°N, 241.4°E)	(25, 9)	60 × 60
	c90		(37, 13)	90 × 90
	c180		(73, 25)	180 × 180
HS	c48	(15.8°N, 153.6°E)	(17, 17)	48 × 48
	c90		(31, 31)	90 × 90
Vortex	c120	(27.2°N, 198.0°E)	(23, 96)	48 × 48
		(24.4°N, 198.0°E)	(27, 96)	
		(28.7°N, 189.6°E)	(23, 85)	

nested-grid model produces satisfactory solutions, while using only simple nested-grid BCs and two-way updating methods. Our boundary conditions are simply linearly interpolated from the coarse-grid data, for all prognostic variables (including the half-time-level C-grid winds) into the halo (ghost) cells of the nested grid.

Nested-grid models typically use what we will refer to as ''serial'' nesting, in which each deeper level of nesting is integrated after its parents on the same set of processes. This process can be inefficient on parallel computers when the nested grid requires much less computational effort than its parent, which is particularly apparent in a global-to-regional nested model where the nest may only cover only a few percent of the global domain's area. We will instead use what we refer to as ''concurrent'' nesting, in which both the coarse and nested grids are run simultaneously on different sets of processors. Concurrent nesting allows us to choose the optimal number of processors (or more precisely, processor cores) for each grid so that a balance can be achieved between distributing a grid to as many processors as-possible, and minimizing message passing and idle processors. Since all grids will be at the same model time, unlike in serial nesting, we linearly extrapolate from two previous coarse-grid solutions to compute the nested-grid BCs at each of the nested-grid's time steps. (In tests with serial nesting, the nested-grid BCs are linearly interpolated in time.) An algorithm describing the concurrent nesting process is given in the appendix for a grid that may be a parent, nest, or both.

Mass-conserving two-way update methods do exist (cf. Zhang et al. 1986; Kurihara et al. 1979; Berger and Colella 1989), but these require computation of integrals for the update and the use of interpolated fluxes at the nested-grid boundary to correctly conserve mass. We use a much simpler approach: since δp is the mass of each layer, we simply do not include it during the two-way update. The coarse-grid pressure is undisturbed during the update and mass is trivially conserved. However, since δp also determines the vertical coordinate (even after vertical remapping, since the surface pressure gives the lowest coordinate surface) a consistent update requires us to remap the other variables—u, v, and Θ—from the nested-grid to the coarse-grid coordinates, using an appropriate extrapolation if the nested-grid surface pressure is less than the coarse-grid surface pressure. Since two-way updating already overspecifies the coarse-grid solution, and since pressure is tightly coupled to the other variables, we expect that not updating δp will not substantially degrade the coarse-grid solution. All simulations described in this paper will use this ''mass-conserving remapping update,'' and are all observed to conserve mass on the coarse-grid to machine precision. Since the horizontal discretization of the FV core does not exactly conserve momentum or total energy we make no attempt to do so in our nesting methodology. Conservation of microphysical species or tracer mass is outside the scope of this study.

Two-way updating is done using temperature $T = \Theta(p/p_0)^{R/c_p}$, where R is the gas constant, c_p is the specific heat at constant pressure, and p_0 is a constant reference pressure, instead of Θ. Updating T was found to yield fewer grid artifacts, likely because unlike Θ it is not a direct function of pressure. The update is a simple areal average with each cell weighted equally: the updated coarse-grid cell-averaged temperature is the average of that of the r^2 corresponding nested-grid cells it is split into. For the winds, we perform a piecewise-constant finite-volume average of the r nested-grid-cell faces along the coarse-grid face whose D-grid wind is being updated. This averaging update is more consistent with our finite-volume discretization than a simple pointwise average would, and the use of piecewise-constant finite-volume averages for the winds means that the update conserves vorticity.

While the nested model can use any integer value for the refinement ratio r, we will use a factor of 3, unless otherwise noted.

It has been noted (Oliger and Sundström 1978; Tribbia and Temam 2011) that open boundary conditions for the hydrostatic primitive equations, such as those applied at our nested-grid boundary, are mathematically ill posed and susceptible to grid-scale noise. We will see that the amount of small-scale noise in our nested-grid simulations is in fact quite small, which is likely due to a combination of the implicit damping in our numerical method, both in the horizontal transport and vertical remapping, and the use of divergence damping. Indeed, Temam and Tribbia (2003) found that a small amount of numerical diffusion applied to the hydrostatic vertical momentum equation resolved the ill posedness of open boundaries and substantially reduced the amount of grid-scale noise in their 2D simulations.

3. Test cases

a. Shallow-water tests

We present three tests of the shallow-water version of the FV core that evaluate the nested model's ability to preserve the desirable large-scale characteristics of the single-grid's solution. Convergence tests are also performed for two of these test cases; neither test case uses a monotonicity constraint so the results can be more easily compared against those found by other shallow-water solvers. Convergence tests are performed using a range of resolutions, from c24—in which each face of the cubed sphere is spanned by 24 grid cells in both directions, for a total of $6 \times 24^2 = 3456$ cells over the entire domain—to c180, representing a range of average grid cell widths from 400 to 50 km, or from 4° to 0.5°. Since the features in these test cases are well-resolved even at a coarse c36 resolution, we do not expect that the nested grid can improve these simulations; indeed, since the solutions are largely in geostrophic balance the discontinuity created by the nested grid will cause greater errors. A nested-grid simulation should instead keep the increase in error to a minimum, and should not converge more slowly than a single-grid simulation.

The FV core becomes a shallow-water model when run with a single layer, a uniform potential temperature, and with the assumption that there is no stress from an overlying layer. Vertical remapping is unnecessary, and when performing mass-conserving two-way updating u and v are updated directly to the coarse grid.

1) BALANCED GEOSTROPHIC FLOW

Test case 2 of Williamson et al. (1992) is a flow initially in geostrophic balance, so any deviations from the initial condition are considered errors. This test is sensitive to spatial changes in grid structure and in particular to the abrupt refinement at the nested-grid boundary. We present tests of the model using a c48 grid in which errors are characterized as the difference between the analytic initial condition and the solution at day 5. The simulation uses an internal "large" time step of 30 min, identical on both grids, corresponding to the interval between vertical remappings in a three-dimensonal model and to the interval between times used for the nested-grid BCs and for performing two-way updates. The coarse grid uses four "small" time steps per large time step, each corresponding to $\Delta\tau$ for one advance of the dynamics, so the time step for the dynamics is 7.5 min. The simulations in this section use fluxes computed by a modification of Suresh and Huynh (1997) as in PL07, with no monotonicity constraint. The nested grid (depicted by a quadrilateral in Fig. 3 and subsequent figures; see also Table 1) is centered in one of the equatorial panels of the cubed sphere, and is a refinement of the coarse grid by a factor of 3 ($r = 3$). The nested grid uses 12 small time steps per large time step. Two flows whose initial height fields [equal to $\delta p/g$ and sampled from the analytic initial condition of Williamson et al. (1992)] are depicted in Fig. 3, are used: one with a purely zonal flow and a more

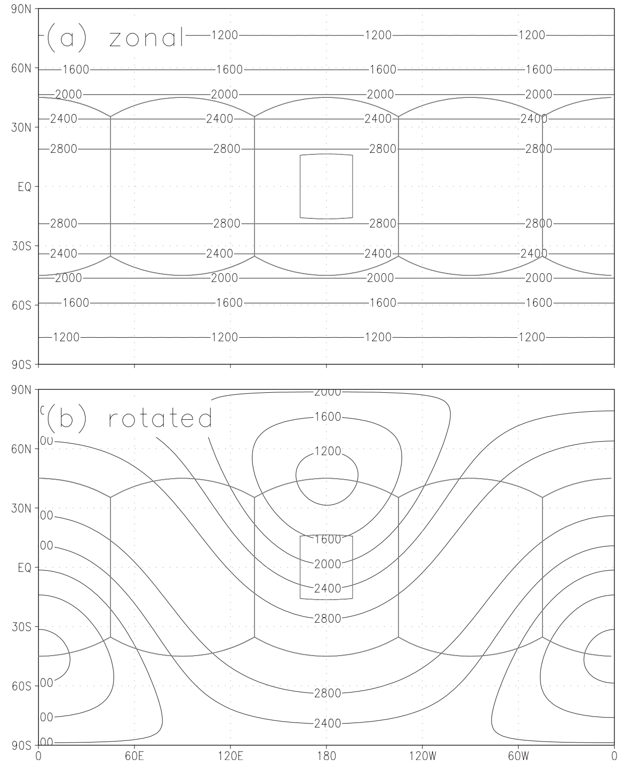

FIG. 3. Initial height field for the shallow-water balanced geostrophic flow test (Williamson test case 2). Contour interval is 400 m. "Rotated" in (b) refers to the flow rotated 45° from zonal. In this and all other figures gray curves indicate boundaries of the cubed-sphere panels and of the nested grid, when present.

TABLE 2. 5-day error norms for c48 simulations of the shallow-water balanced geostrophic flow test (Williamson test case 2).

	Zonal			Rotated		
	ℓ_1	ℓ_2	ℓ_∞	ℓ_1	ℓ_2	ℓ_∞
Single-grid c48	3.28×10^{-5}	3.97×10^{-5}	2.81×10^{-4}	4.83×10^{-5}	6.68×10^{-5}	6.35×10^{-4}
Nested-grid c48	3.85×10^{-5}	4.52×10^{-5}	3.27×10^{-4}	9.10×10^{-5}	1.29×10^{-4}	6.36×10^{-4}

stringent test with a flow field rotated 45° from zonal to allow the strongest part of the flow to pass over the corners of the cubed sphere and of the nested grid.

We compute the area-weighted error norms:

$$\ell_1 = \frac{\sum(hA - h_{\mathrm{IC}}A)}{\sum(h_{\mathrm{IC}}A)} \quad \ell_2 = \frac{\sum(hA - h_{\mathrm{IC}}A)^2}{\sum(h_{\mathrm{IC}}A)^2}$$
$$\ell_\infty = \frac{\max(hA - h_{\mathrm{IC}}A)^2}{\max(h_{\mathrm{IC}}A)^2}, \tag{6}$$

where h, h_{IC}, and A are the height, initial height, and area of each cell, respectively, and the sum and maximum are over all grid cells on the coarse grid. All error norms are computed on the native cubed-sphere grid. Note that hA is proportional to the mass in each grid cell.

Even the largest ℓ_1 and ℓ_2 error norms (Table 2) in our c48 simulations are still very small, with only one (the nested-grid rotated flow simulation) being over one part in 1000. The exception is the ℓ_∞ norm, which is dominated by the nearly singular edges of the cubed sphere and so does not decrease with grid spacing. The cubed-sphere grid structure is apparent in the error field (Fig. 4). Improvement of the numerical scheme at the edges of the cubed sphere is a topic for further research. Using grid nesting in the zonal flow test cases only increased the error norms by at most 20%. In the more stringent rotated flow test case, the nested-grid simulation's error norms were double that of the single-grid simulation, except for the ℓ_∞ norm, which is nearly identical in the two simulations. Using serial nesting instead of concurrent nesting in the rotated flow case changes the ℓ_1 and ℓ_2 error norms by at most 0.05% in either direction, with larger effects (particularly at low resolution) for the ℓ_∞ norm. Also in the rotated flow case error norms increased by no more than 5% for refinement ratios of 2, 4, and 8 compared to our factor-of-three refinement, and error norms only increased by a factor of a third over the factor of 3 refinement when a refinement ratio of 16 was used.

The unstructured-grid model of Ringler et al. (2011) with a locally refined region had 12-day global ℓ_2 errors

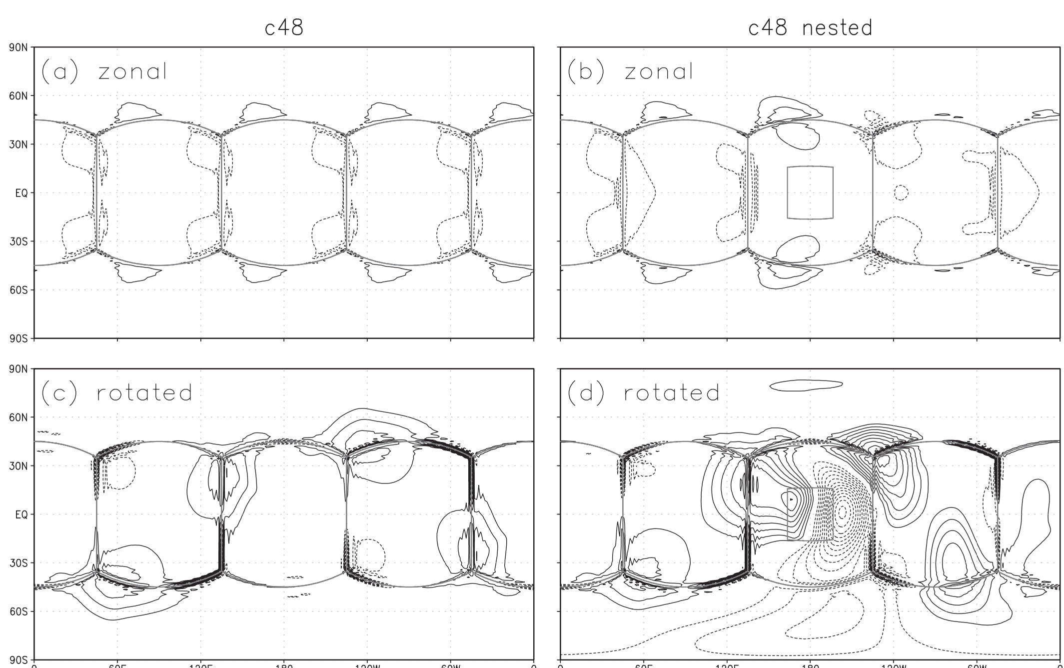

FIG. 4. Absolute 5-day height errors for the shallow-water balanced geostrophic flow test (Williamson test case 2) on a c48 coarse grid. Contour interval is 0.1 m, negative values dashed, and zero contour suppressed.

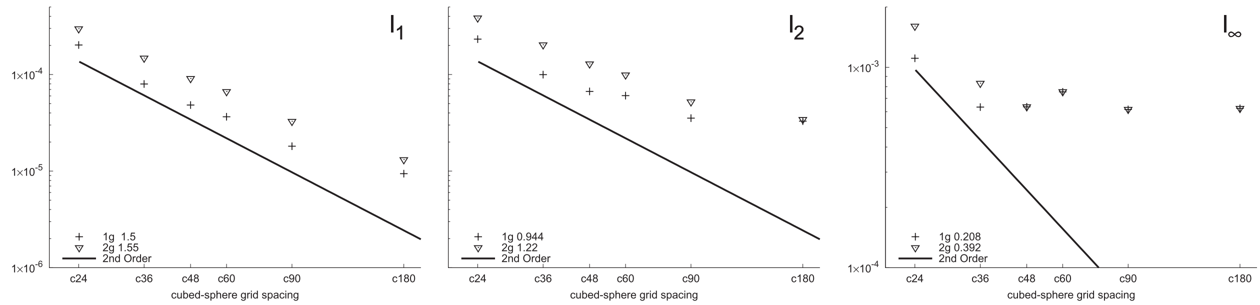

FIG. 5. Convergence of absolute 5-day height errors for the rotated shallow-water balanced geostrophic flow test (Williamson test case 2). Empirical convergence rates are given in the legends. Tests are performed without a monotonicity constraint. Note the different vertical axis for the ℓ_∞ norm.

progressively increasing with greater refinement, so that the error norm with a mesh-size variation of 16 was an order of magnitude larger than that the uniform-resolution simulation. Weller et al. (2009) tested a number of different grid geometries in the Atmosphere Field Operation and Manipulation (AtmosFOAM) model, and found that errors increased by as much as a factor of 2 when refining a hexagonal grid, and relatively minimal increases in errors when refining a cubed-sphere grid or a triangular grid. The adaptive finite-volume simulation of St-Cyr et al. (2008), which used a gradual factor of 4 refinement, found the ℓ_2 error in a $\alpha = \pi/4$ simulation to increase by a factor of about 2.5 compared to a uniform-resolution simulation, but in simulations using sixth-order spectral elements the error was halved in a refined simulation compared to a uniform-resolution simulation.

An empirical convergence rate can be computed by performing simulations across a range of resolutions, from c24 (roughly 400-km grid spacing) to c180 (50-km grid spacing) and using a least squares fit to the error norms as in Harris et al. (2011). The results for the rotated flow test are depicted in Fig. 5. In the ℓ_1 norm the rotated flow case converges at an order of about 1.5 for both the single- and nested-grid simulations; for the zonal flow case the convergence rates are about 1.7. The other error norms show more impact from the singular grid edges, which causes a loss of convergence in the ℓ_2 norm at c180 resolution, and little convergence in the ℓ_∞ norm. That the nested-grid solutions have nearly identical ℓ_∞ norms at c48 and higher resolutions indicates that the error in this norm is primarily due to the coarse-grid's edges and not to nested-grid artifacts. Disregarding the c180 simulation would yield convergence rates of about 1.7 in the ℓ_1 norm for both flows and both single- and nested-grid simulations, and of about 1.4 in the ℓ_2 norm. In the zonal flow cases the ℓ_2 norm convergence rate is about 1.3, including the c180 simulations at which convergence begins to degrade. Convergence rates were little changed when refinement ratios of 2 or 4 were used.

The unstructured-grid model of Ringler et al. (2011) found a qualitative convergence rate between first and second order in the ℓ_2 norm for locally refined regions with refinement ratios between 2 and 16, but with slower convergence at higher resolutions. Weller et al. (2009) considered a variety of uniform-resolution and refined global grids and found roughly second-order accuracy in the ℓ_2 norm in all cases. Lee and MacDonald (2009) achieved second-order convergence in their uniform-resolution icosahedral model in all three error norms, and Li et al. (2008) found varying convergence rates between first and third order in all three error norms for their multimoment model on the Yin–Yang grid. Ullrich et al. (2010) found convergence rates nearing fifth order using a fourth-order finite-volume method on a cubed-sphere grid, using a special remapping procedure to limit errors due to the cube edges.

2) ISOLATED MOUNTAIN TEST CASE

A more complex test of the shallow-water solver is Williamson test case 5, in which an initially uniform geostrophic flow impinges upon a synoptic-scale mountain in the midlatitudes to create a Rossby wave train. This test case is more nonlinear than is test case 2, and as a consequence there exists no known exact solution. We will therefore use the output of a high-resolution c720 simulation, with roughly 12-km grid spacing, as our reference solution against which error norms can be computed. The simulations presented in this section also use fluxes computed from PL07's modification to Suresh and Huynh (1997). Also, in this section we use $\beta = 0.4$, the same as in Chen and Lin (2011), which yields smaller error norms in this test case.

The coarse grid is rotated so that the center of one of the cubed-sphere panels is located over the mountain, which is at 30°N, 90°W. In nested-grid simulations the nest is centered over the mountain as well; for this test

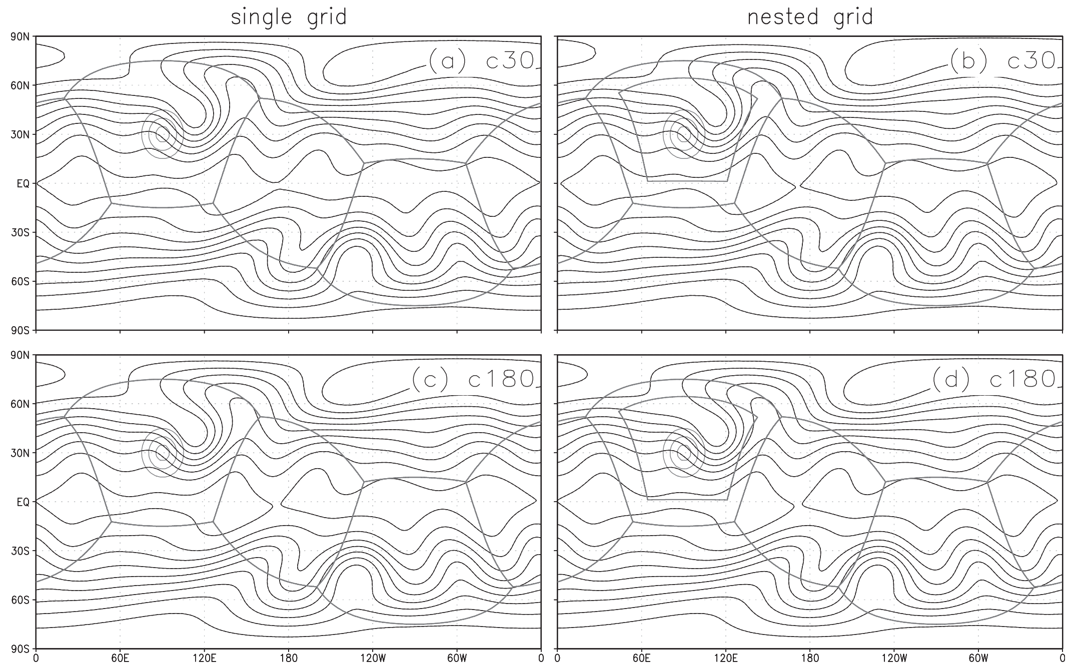

FIG. 6. 15-day total height for the isolated mountain test case (Williamson test case 5). Contour interval is 100 m; topography indicated by light gray lines, with contour interval 500 m.

case, the nested grid has been enlarged to cover the entire mountain. No smoothing is applied to the topography, although the results were little changed when using topography with a continuous third derivative. The error norms are computed as in (6), with h_{IC} replaced with the height field of a c720 control simulation, using an area average to bring the control solution to the same resolution as the coarse grid of the simulation being evaluated. All analyses for this test case use the total height of the fluid surface: the height of the topography plus the fluid depth.

The total height field (Fig. 6) is nearly visually indistinguishable between our simulations for resolutions better than c30, a result also found by LR97, Li et al. (2008), and Lee and MacDonald (2009). The same is true for the zonal wind fields (not shown). The total height field in the nested-grid simulations are little different from those in the single-grid simulations of the same resolution. The height differences at day 15 between two lower-resolution simulations and the c720 control simulation are shown in Fig. 7. In this test case, the cubed-sphere artifacts are more difficult to see as the error is dominated by phase errors in the lee waves. Some nested-grid artifacts are visible, particularly at latitudes north of the mountain. The amplitude of the nested-grid artifacts decrease with increasing resolution, so that at c180 resolution the error norms (Fig. 8) are nearly identical in the single- and nested-grid simulations. A consequence of this reduction in nesting artifacts is that the empirical convergence rate, which falls short of first order in the single-grid simulations, is increased in the nested simulations to roughly first order.

A few studies give error norms and convergence rates for this test case. Ringler et al. (2011) found a convergence rate qualitatively between first and second order in the ℓ_2 norm, and that the errors were slightly smaller when using a refined grid. Weller et al. (2009) found uneven ℓ_2 convergence rates between first and second order for a variety of grid geometries, and that refinements either increased or decreased the error norms.

3) ROSSBY–HAURWITZ WAVE

The Rossby–Haurwitz wave, Williamson test case 6, is most interesting because the wavenumber-4 Rossby–Haurwitz wave is unstable (Thuburn and Li 2000), and truncation and round-off errors will eventually grow and cause the wave to break. Thus, the time that the model can maintain the wave is a useful measure of how quickly the model allows numerical errors to grow to large amplitude. While the FV core maintains the wave well beyond 60 days even at coarse resolutions—LR97 demonstrated stability through 60 days even for a 2.5° resolution simulation, which we have also found for a c48 cubed-sphere simulation—many other *uniform-resolution* global models do not claim stability beyond 14 days (cf. Lee and MacDonald 2009; Li et al. 2008;

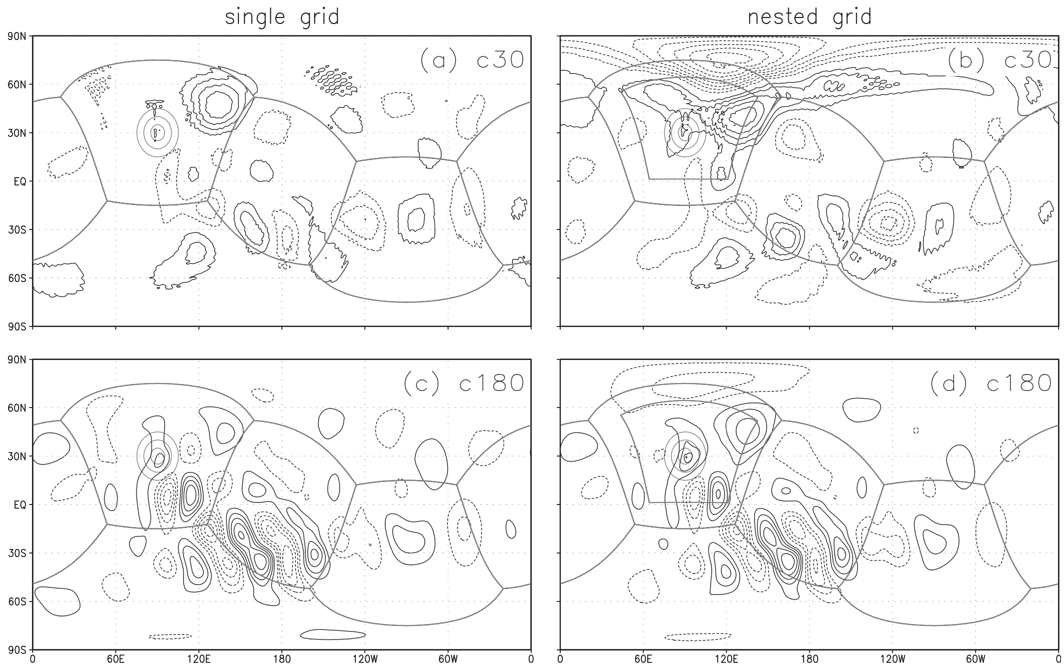

FIG. 7. Absolute 15-day total height errors for the isolated mountain test case (Williamson test case 5). Contour interval is 5 m for the c30 simulations and 1 m for the c180 simulations, negative values are dashed, and the zero contour is suppressed. Topography indicated by light gray lines, with contour interval 500 m.

Bernard et al. 2009). Longer stability times are found in other uniform-resolution global models, including those of Rossmanith (2006) and Ullrich et al. (2010). While we do not expect our nested-grid model to preserve the wave for longer than a few weeks because of the unavoidable error introduced by the nested grid, we expect to retain stability at a low c48 resolution for at least 14 days, and longer at higher resolutions.

The c48 test case uses the same parameters as for the balanced geostrophic flow test case. The two-way nested solution then maintains the wave for 14 days and later breaks down. If instead we use a c180 grid, in which the large time step is reduced to 5 min on both grids and the nested grid made 180 grid cells wide in both directions (so as to cover nearly the same area as in the c48 simulations), the wave is better maintained at 14 days and does not break until after 21 days.

b. Jablonowski–Williamson baroclinic instability test

The baroclinic instability test case of Jablonowski and Williamson (2006) is a common test for three-dimensional global models to show that a reasonable baroclinic wave can be simulated in a perturbed baroclinically unstable flow. In our nested-grid simulations we wish to show that two-way nesting does not appreciably distort the synoptic-scale baroclinic wave compared to a single-grid solution, and that nesting permits finer-scale features to be represented in the solution.

The initial condition is as in Jablonowski and Williamson (2006). The cubed sphere is rotated so that

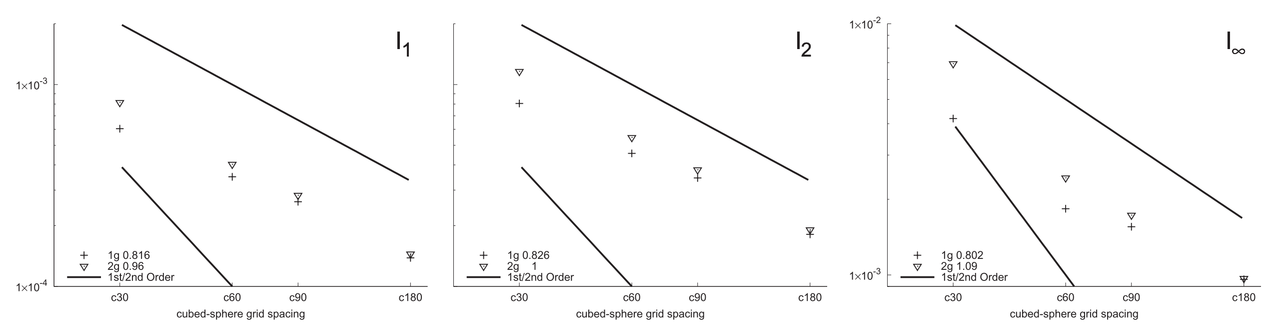

FIG. 8. Convergence of absolute 15-day height errors for the isolated mountain test case (Williamson test case 5). Empirical convergence rates are given in the legends. Tests are performed without a monotonicity constraint. Note the different vertical axis for the ℓ_∞ norm.

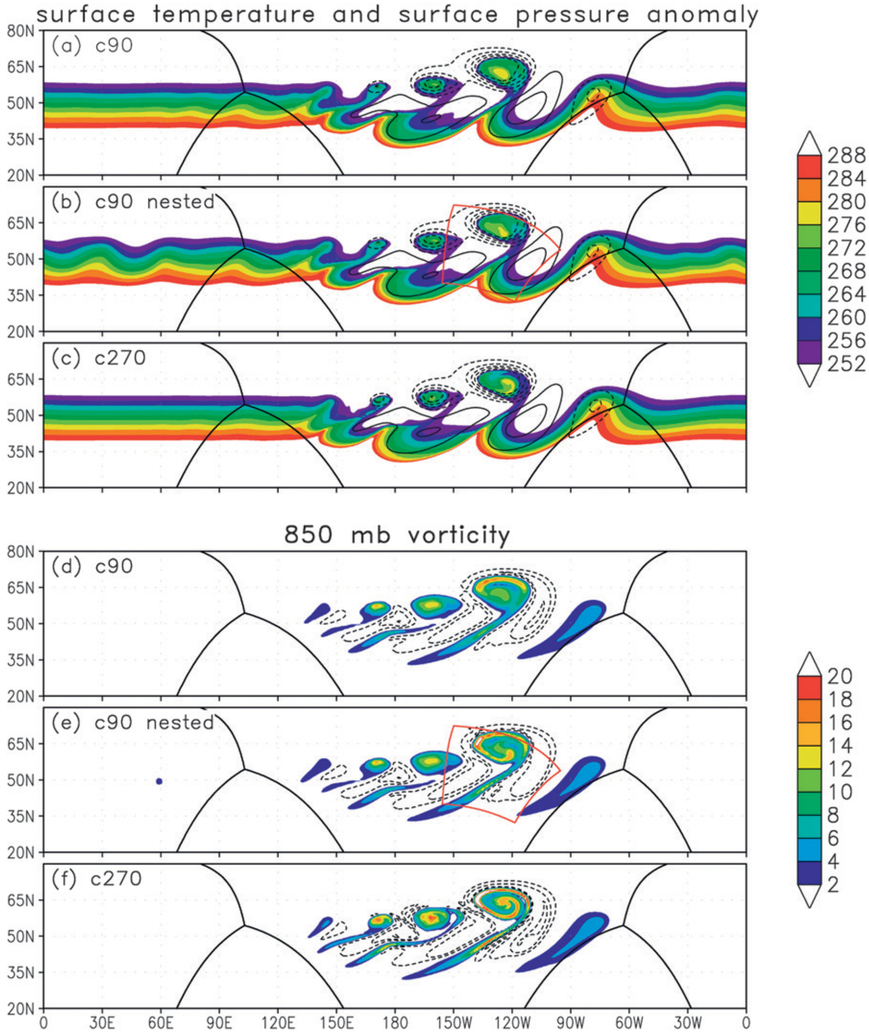

FIG. 9. Jablonowski–Williamson test case solutions at day 10 for (a),(d) a single-grid c90 simulation; (b),(e) a nested-grid c90 simulation; and (c),(f) a single-grid c270 simulation. In (a)–(c) surface temperature (K, color) and pressure perturbation (contour interval 4 hPa, negative values dashed) are shown; in (d)–(f) 850-hPa absolute vorticity (positive values in color, negative values contours of interval $2 \times 10^{-5}\ \mathrm{s}^{-1}$) is shown. Here, the nested grid is outlined in red.

the initial perturbation, at 40°N, 20°E, is centered in one of the panels. The nested grid (seen in Fig. 9) is then placed so that it covers the deepest low in the resulting baroclinic wave train at $t = 10$ days.

Our c90 simulations use a large time step of 20 min on both grids, with 10 and 21 small time steps per large time step on the coarse and nested grids, respectively. The nested grid is a 3:1 spatial refinement of the coarse grid and is 90 grid cells wide in both directions. The model uses the same 32-level vertical discretization as in Zhao et al. (2009) and in Chen and Lin (2011).

Results of the c90 simulations are seen in Fig. 9. The nested grid is not causing any obvious distortion of the baroclinic wave compared to the single-grid c90 solution; furthermore, the low center is more tightly rolled in the nested-grid simulation, as best seen in the vorticity field (Figs. 9d–f). This is made more apparent by examining a close-up of the low (Fig. 10). A single-grid c270 simulation—one with the same resolution globally as does the nested grid in the c90 simulation—shows a low which is even more tightly wrapped than the c90 nested-grid simulation. Since the tests of Jablonowski and Williamson (2006), and a similar set of tests in L04, show that the low in these test cases becomes more tightly wrapped with increasing resolution, we expect the c270 simulation to be more tightly wrapped than either c90 simulation; however, introducing grid nesting in the c90 simulation allows more of the roll-up to appear

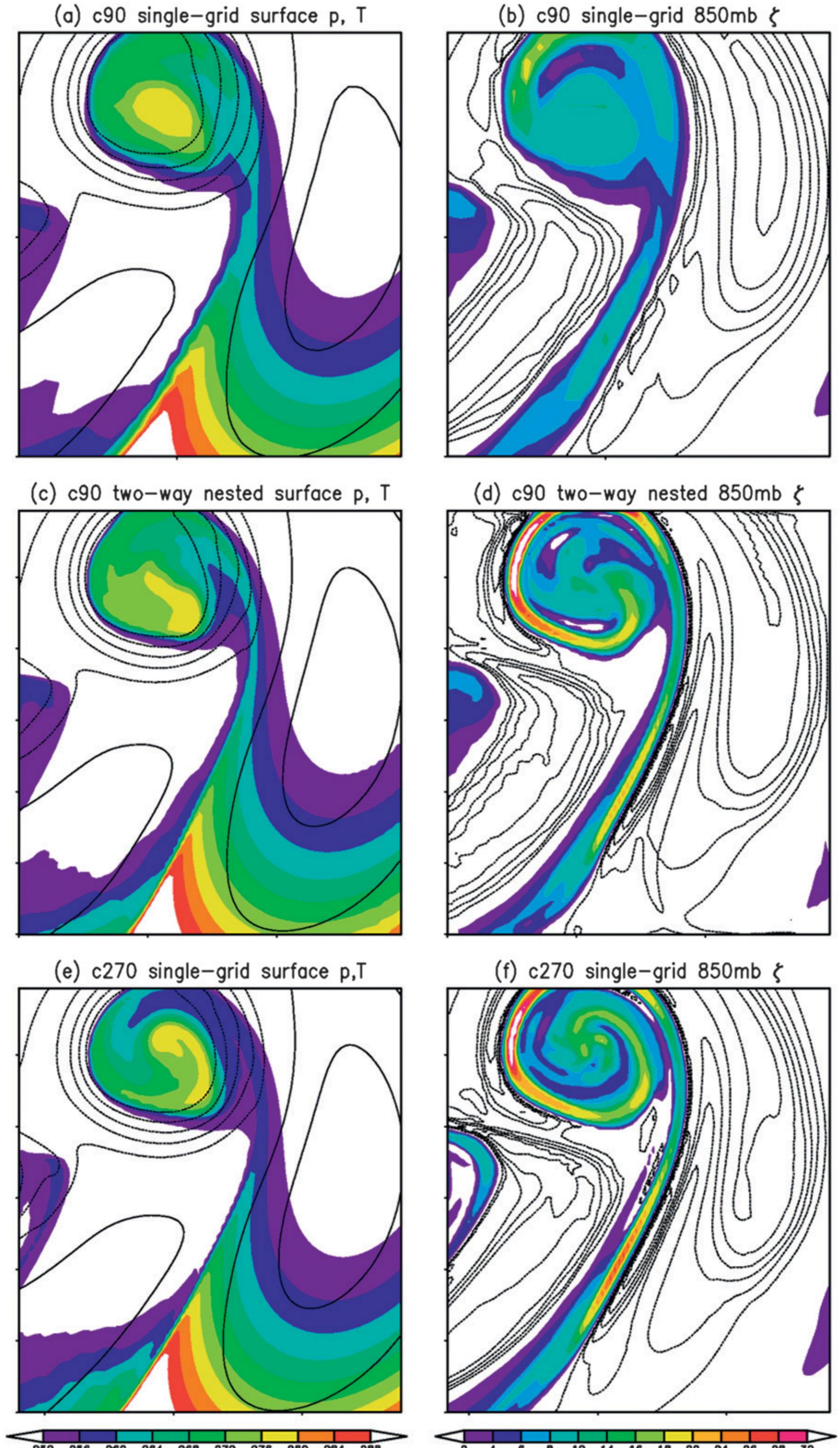

FIG. 10. Jablonowski–Williamson test case solutions at day 10 on the (a),(b) single-grid c90 simulation; (c),(d) nested grid of a two-way c90 simulation; and (e),(f) the c270 single-grid simulation. In (a),(c),(e) surface temperature (K, color) and pressure perturbation (contour interval 4 hPa, negative values dashed) are shown; in (b),(d),(f) 850-hPa absolute vorticity is shown (positive values in color, negative values contours of interval 10^{-5} s^{-1}; note that the contour interval of the negative values is smaller than that of the positive values, to show detail in the vorticity field).

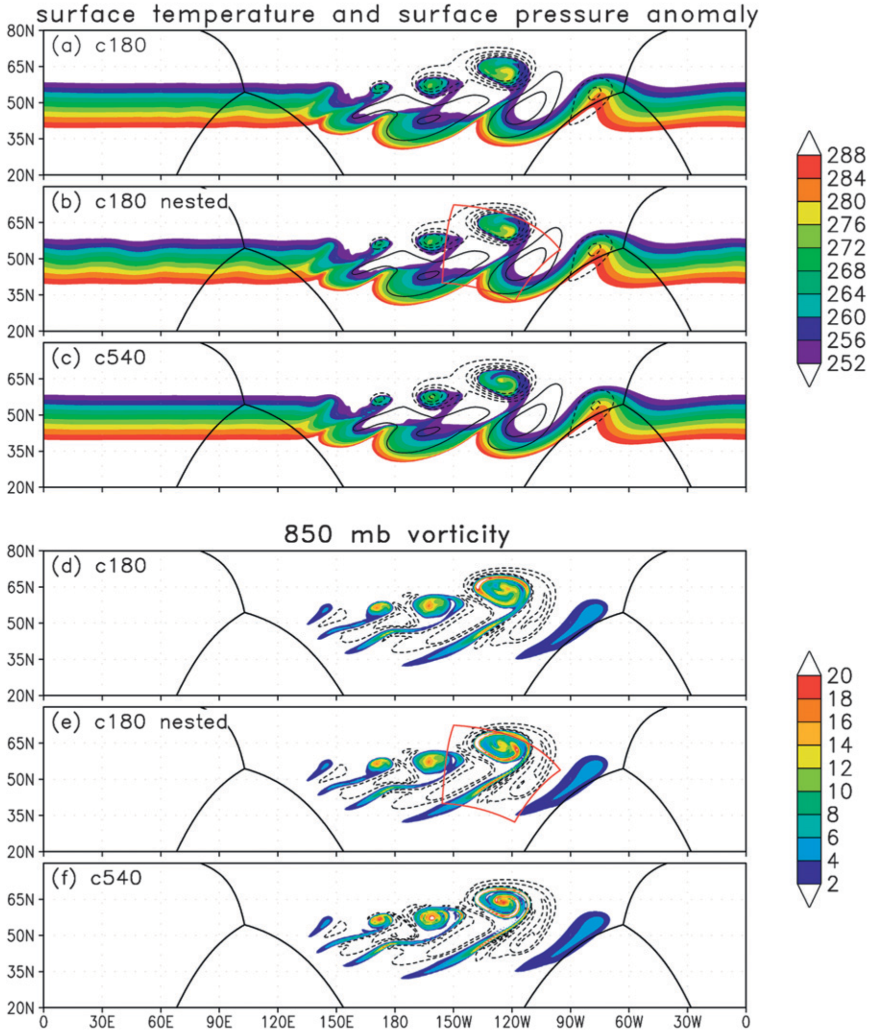

FIG. 11. As in Fig. 9, but at (a),(b),(d),(e) c180 resolution and (c),(f) c540 resolution.

than does a simulation without nesting. Examination of the nested-grid solution (Figs. 10c,d) does show some low-amplitude distortion of the solution near the nested-grid boundary compared to the c270 simulation (Figs. 10e,f), particularly in the vorticity field, but this does not substantially affect the solution. The nested-grid solution preserves the strong gradients along the cold front, demonstrating that the FV core's maintenance of sharp gradients (cf. LR97, section 4) is sustained in a nested-grid simulation. However, the nested grid causes little improvement of the solution elsewhere. The two c90 solutions are nearly identical outside of the nested region, save for a propagating nested-grid artifact visible in the temperature field at 30° longitude (Fig. 9e).

A series of c180 simulations were performed (Fig. 11) using the same model parameters as the c90 simulations except that the large time step was 10 min on both grids and used a nested grid 180 cells across to cover approximately the same area as in the c90 nested simulation. The nested-grid solution is no worse than the single-grid c180 solution, and the fine structure inside the deepest low is more tightly wound in a nested-grid c180 simulation, although not as much as it is in the c540 control simulation. Outside of the nested region there is no improvement to the solution.

The error introduced by grid nesting can be quantified by comparing solutions to a high-resolution solution taken as "truth." As in Jablonowski and Williamson (2006) we will compute ℓ_2 error norms in the surface pressure field on the global grid as a function of time; the norms are computed as in (6) but with h replaced by surface pressure p_s and h_{IC} replaced with the surface pressure from a c540 reference simulation, using an area average to bring the c540 solution to the same resolution as the

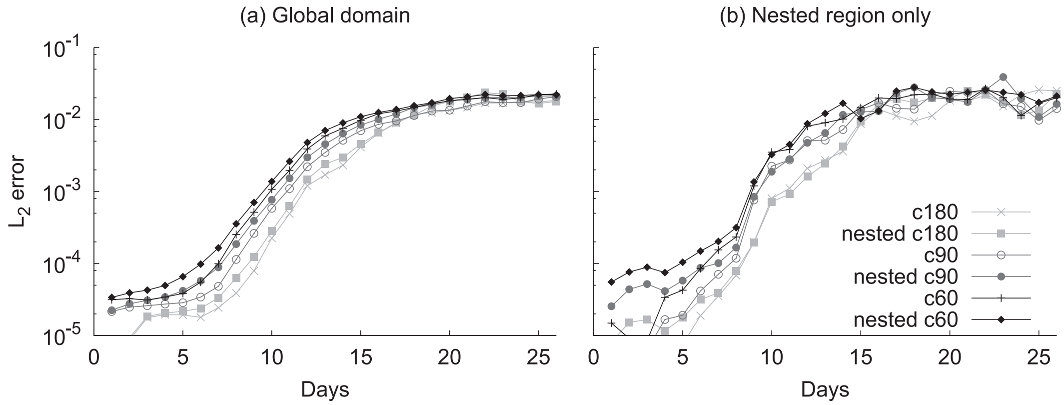

FIG. 12. Jablonowski–Williamson test case surface-pressure ℓ_2 errors relative to a c540 simulation over (a) the entire global domain and (b) the part of the coarse grid covered by the nested grid. Note the logarithmic scaling on the vertical axis.

coarse grid of the simulation being evaluated. For comparison, we have also performed a pair of c60 simulations; in all nested simulations the nested grid is at the same location. Both the single-grid and nested-grid solutions show increasing error growth during the first two weeks of the simulation (Fig. 12a) before the error ''saturates'' as both the reference and the lower-resolution simulations equilibrate and mix out their potential vorticity gradients. Both single- and nested-grid simulations show convergence at increasingly high resolutions, with only a slight increase in error and no pathological error growth due to the nested grid. The difference between the nested and single-grid simulations is greatest in the first week of the simulation; as a result of the impulsive start of the model and the small initial perturbation used to excite the baroclinic wave, artifacts from the nested grid will dominate the error at early times. Indeed, the percent increase of the error norm compared to the equivalent single-grid simulation is at its greatest during the first week of the simulation, although even at their greatest the nested-grid simulations' global error norms are less than twice that of the single-grid simulation. From day 9 onward, the error norms in the nested-grid simulation are no more than 40% greater than those in the corresponding single-grid simulation. The effect of grid artifacts is even more apparent for errors computed only over the nested region (Fig. 12b). During the first week these artifacts are the only disturbances to the initial condition in the nested-grid region. Once the wave enters the nested grid, the nested-region error norms in a nested-grid simulation are more similar to those in a single-grid simulation, with increases in the nested-grid simulations' error norms being no more than 20% between days 9 and 12, and on day 10 the errors are modestly (5%–20%) lower for all three nested-grid simulations; in the c180 simulation the lower errors are sustained through day 13. The errors are found to increase at $t = 10$ days when using serial instead of concurrent nesting, although by less than 1% globally and less than 5% over the nested region. Using a refinement ratio of 2, or decreasing the large time step (while also decreasing the number of small time steps, so as to hold the small time-step length constant) caused little change to the error norms except very early in the simulation, when the error is dominated by startup noise, or very late once the error has saturated. Note that in all of the simulations the error norms computed over the entire domain are typically smaller than those limited to the nested-grid region, since error norms are defined as area averages and much of the global domain, including the entire Southern Hemisphere, has much lower errors than the active region covered by the nested grid.

c. Held–Suarez climate integration

An important test for global dynamical cores is a multiyear climate integration using the Held–Suarez forcing (Held and Suarez 1994) to simulate the effects of idealized, zonally symmetric diabatic heating and surface drag in a dry dynamical core. Here, we will evaluate the impact of a nested grid on the climate statistics compared to a single-grid model. We first present results from a pair of c48 simulations, which use the same grid (and indeed the same dynamical core) as in the Geophysical Fluid Dynamics Laboratory Atmospheric Model version 3.0 (GFDL AM3; Donner et al. 2011) model, and has an average gridcell width of about 200 km. The large time step is 20 min on both grids, with 4 and 12 small time steps per large time step on the coarse and nested grids, respectively. The remainder of the model configuration is as for the Jablonowski–Williamson test cases, except that the model grid is not rotated, and that the nested grid is again centered in an equatorial panel.

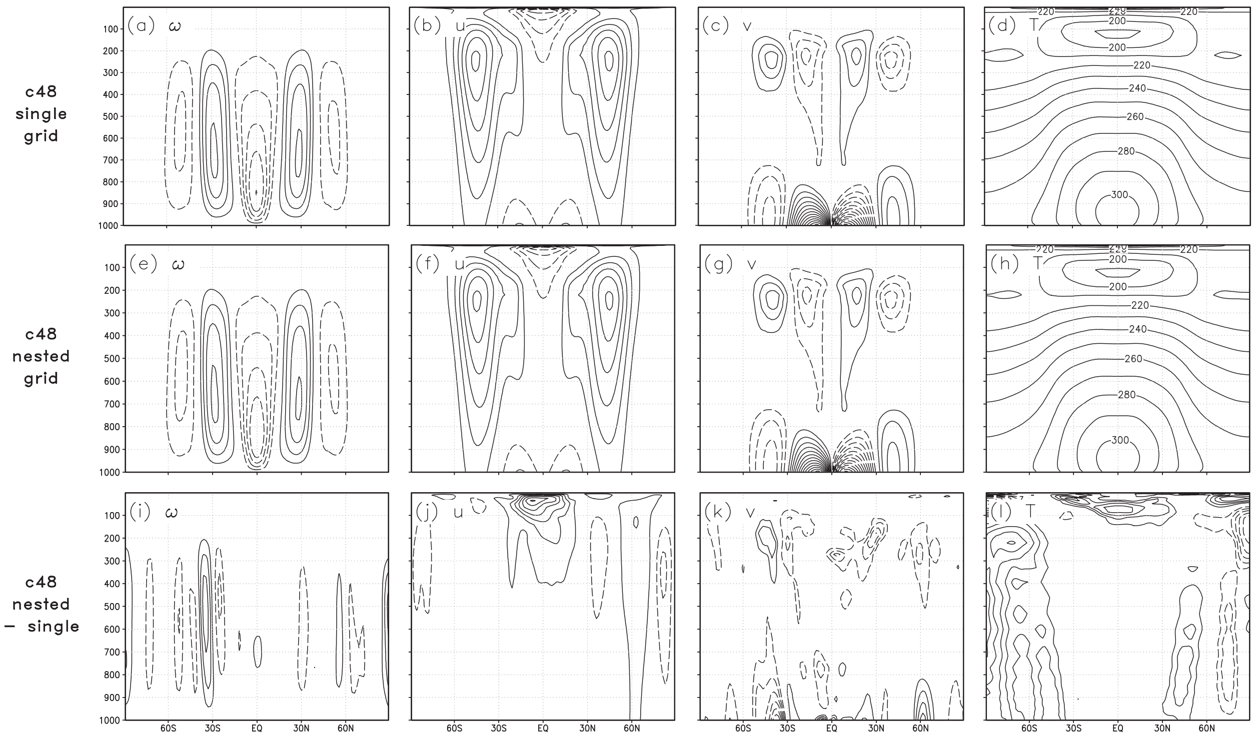

FIG. 13. 2000-day-averaged c48 Held–Suarez simulation zonal means: single-grid simulation (a) ω (contour interval 5 hPa day^{-1}), (b) u (5 m s^{-1}), (c) v (0.25 m s^{-1}), and (d) T (10 K). (e)–(h) As in (a)–(d), but for the nested-grid simulation. (i)–(l) The difference between the nested and coarse-grid simulations is depicted; contour intervals are (i) 0.25 hPa day^{-1}, (j) 0.25 m s^{-1}, (k) 0.005 m s^{-1}, and (l) 0.05 K. In all panels negative values are dashed and the zero contour has been suppressed.

Zonal means over a 2000-day period from c48 simulations, after a 200-day model spinup period, are shown in Fig. 13. In Figs. 13a,e,i, the vertical velocity $\omega = dp/dt$ is depicted, computed as in L04, as a useful diagnostic of the strength of the meridional overturning circulations. The zonal means are very similar between the two simulations, and the differences between the simulations (bottom row) are small; the same is true for the eddy covariances (Fig. 14). Note that the greatest difference between the nested and single grid simulations is not in the tropics, where the nested grid is located, but in the midlatitudes, although large differences can be seen in the tropics near the top boundary. The asymmetry between the differences in the Northern and Southern Hemispheres decreases when examining the next 2000 days of the simulations (not shown). Furthermore, there is little difference between our results and those of L04, which used the latitude–longitude FV core: the most apparent difference between our c48 simulations and L04's 2° simulations (of similar resolution) is that our subtropical descent (Figs. 13a,b) is stronger, and our subpolar ascent is weaker. Midlatitude eddy covariances are also slightly stronger in our simulations (Fig. 14), likely due to reduced implicit numerical diffusion in the cubed-sphere core.

Differences between the nested- and single-grid simulations become more apparent when examining deviations from the zonal means, since ideally the time-averaged fields should be zonally symmetric. These asymmetries are most pronounced in the ω field, which shows noticeable errors at the cubed-sphere edges at the surface (Figs. 15a,b) but more prominently at 500 mb (Figs. 15c,d). Asymmetries are also apparent at the nested-grid boundary, which are larger than those at the cubed-sphere edges at the surface but are imperceptible at 500 mb. Other fields show little distortion due to the nested grid: for example, the 500-hPa u (Figs. 15e,f) shows little deviation from zonal symmetry due to grid structure. In both the nested and single-grid simulations the asymmetry between the Northern and Southern Hemispheres, as well as deviations from zonal symmetry, decreases for longer simulations. Tests using a shorter large time step of 5 min, with the small time-step length unchanged, found that the artifacts in the ω field were greatly reduced, although at the added computational expense of more frequent vertical remappings and two-way updates.

Similar results are found from a pair of c90 simulations, which are set up the same as the c48 simulations except that the large time step is now 10 min on both

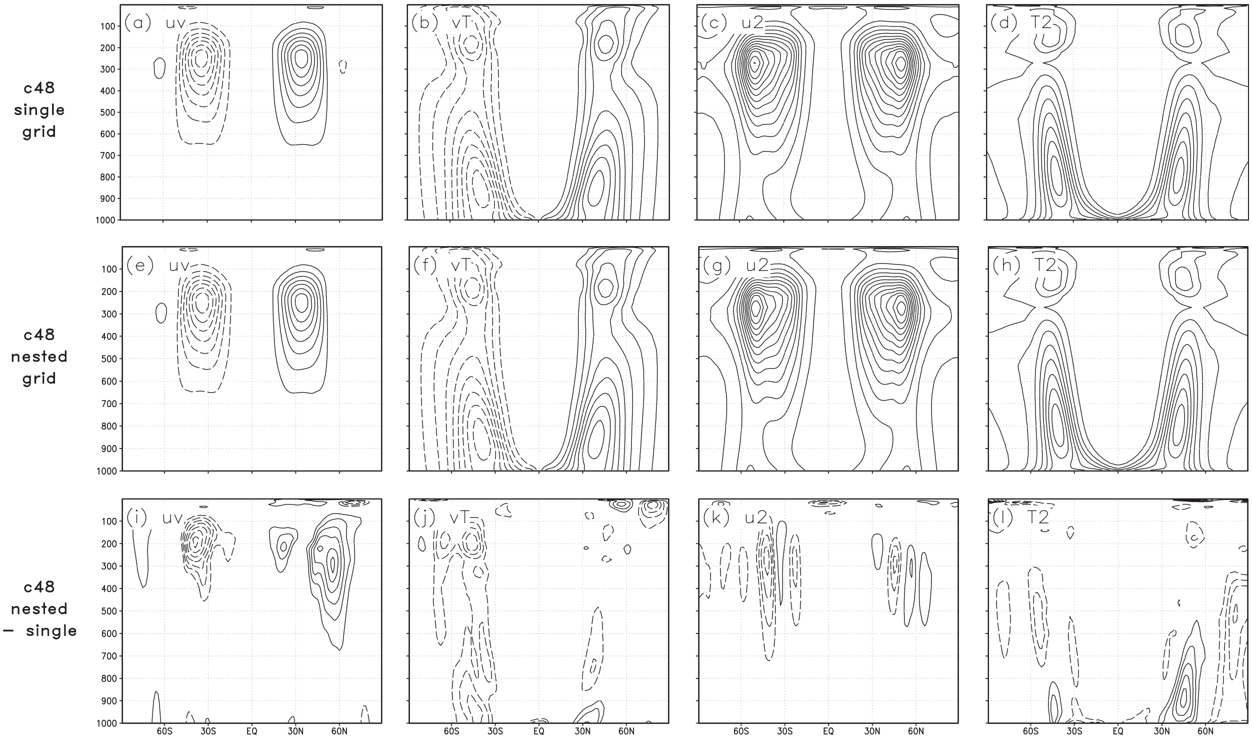

FIG. 14. 2000-day-averaged c48 Held–Suarez simulation eddy statistics: single-grid simulation (a) meridional flux of zonal momentum (contour interval 10 $\mathrm{m^2\ s^{-2}}$), (b) meridional heat flux (2.5 $\mathrm{K\ m\ s^{-1}}$), (c) zonal wind variance (20 $\mathrm{m^2\ s^{-1}}$, largest contour 260 $\mathrm{m^2\ s^{-1}}$), and (d) temperature variance (5 $\mathrm{K^2}$, largest contour 40 $\mathrm{K^2}$). (e)–(h) As in (a)–(d), but for the nested-grid simulation. (i)–(l) The difference between nested and coarse-grid simulation is depicted; contour intervals are (i) 0.2 $\mathrm{m^2\ s^{-2}}$, (j) 0.1 $\mathrm{K\ m\ s^{-1}}$, (k) 2 $\mathrm{m^2\ s^{-1}}$, and (l) 0.2 $\mathrm{K^2}$. In all panels negative values are dashed and the zero contour has been suppressed.

grids. The zonal means and eddy covariances (not shown) are very similar to those in the c48 simulations (Fig. 13). The difference between the nested and single-grid c90 simulations (Fig. 16) is similar to those in the c48 simulations. The greater differences between the nested and single-grid simulations in some fields (particularly ω and uv) at higher resolution may be due to there being more finescale variability in the solution at c90 than at c48. The noise in the ω field (Figs. 17a–d) due to the cubed-sphere edges and nested grid are smaller than in the c48 simulations, and again grid artifacts are imperceptible in other fields (Figs. 17e,f).

d. Lee vortices

The final test simulates vortex shedding in the lee of the Big Island of Hawaii (Smith and Grubišić 1993) to determine whether the nested grid can introduce disturbances downstream of the nest caused by features that would not be resolved by the coarse grid alone. We do not aim to precisely reproduce observed vortices on a particular date, but to instead show that vortices that could not appear in a single-grid simulation can be supported on the coarse grid in a two-way nested simulation. These simulations are initialized using a T574 analysis from the National Centers for Environmental Prediction (NCEP) at 0000 UTC 1 August 2010 and use 1-min U.S. Geological Survey (USGS) topography, averaged to the grid resolution. To prevent surface winds from being unrealistically strong, the surface drag from the Held–Suarez test is applied. Two global grids are used: a c360 simulation with a 5-min large time step and 10 small time steps per large time step, and a c120 simulation with a 10-min large time step and 10 small time steps per large time step. A c120 nested-grid simulation was also performed using a 3:1 spatial refinement, so that the nested grid has the same resolution as the c360 simulation does globally, and 30 small time steps; again, the large time step is identical on the coarse and nested grids. The remainder of the model is formulated as in the Held–Suarez test case.

By $t = 72$ h there is a clear train of lee vortices apparent in the surface vorticity field in the c360 simulation (Fig. 18a), extending west-southwest downstream from the Big Island of Hawaii. Shedding occurs throughout the 96-h-long simulation (Fig. 18f), although the wake is more uniform by $t = 96$ h. We expect that the c120

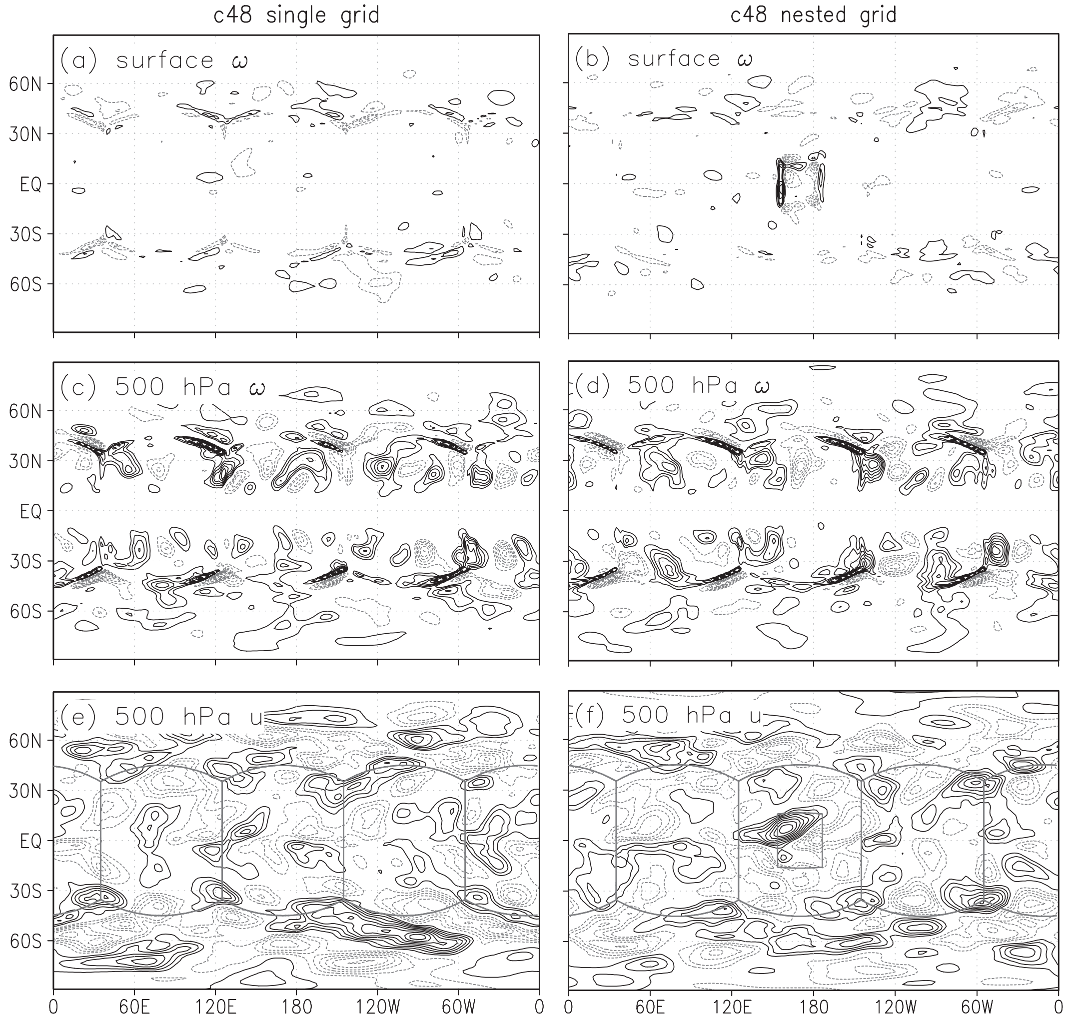

FIG. 15. 2000-day averages, with zonal means removed, for (a),(b) lowest model-level ω/ω_0 (contour interval 0.01); (c),(d) 500 hPa ω/ω_0 (0.1); and (e),(f) 500 hPa u/u_0 (0.01), in c48 (a),(c),(e) single-grid and (b),(d),(f) nested-grid simulations. Characteristic velocities are $\omega_0 = 10$ hPa day^{-1} and $u_0 = 10$ m s^{-1}. In all panels the zero contour has been suppressed for clarity, as has been the grid geometry in (a)–(d), and negative values are plotted in gray.

nested simulation should have vortices form on its nested grid, but we also find that the nested-grid vortices are able to propagate out of the coarse grid and remain coherent downstream (Fig. 18b), and are slowly diffused by the dissipation in the numerics. Again, vortex shedding continues throughout the simulation (Fig. 18g). By contrast, the vortices in the single-grid c120 simulation are much weaker and poorly defined (Figs. 18c,h), indicating that at c120 resolution (roughly 75 km) the 150-km-wide Big Island of Hawaii is not well-enough resolved for the processes producing lee vortices to act. The poorly resolved topography in the single-grid c120 simulation creates much less of the baroclinically produced vorticity needed on the flanks of the island for vortex generation: the absolute value is at most 1.9×10^{-5} s^{-1} at $t = 72$ h, compared to 55.1×10^{-5} s^{-1} in the single-grid c360 simulation and 25.8×10^{-5} s^{-1} on the coarse grid of the nested-grid c120 simulation. (On the nested grid, the maximum vorticity is 74.4×10^{-5} s^{-1}. This value is larger than in the single-grid c360 case because the terrain smoothing is not as strong on the nested grid, and so the mountain is somewhat steeper.) The vorticity that does appear in the single-grid c120 simulation are transients caused by the impulsive startup of the simulation, and continuous shedding does not occur.

To determine whether the vortices in the nested test cases are merely noise generated by the nested-grid boundary, two sensitivity tests were carried out. A test in which the nest was shifted southward, so as to move the sensitive southwest corner of the nest out from Hawaii's wake (Figs. 18d,i), produced a nearly identical solution.

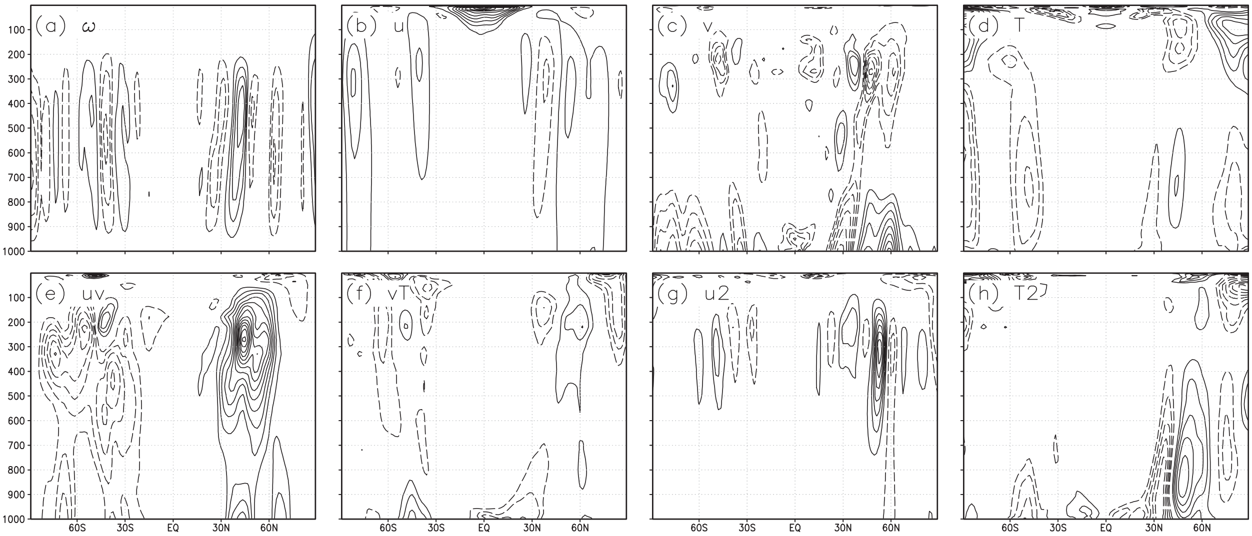

FIG. 16. Difference between c90 nested and coarse-grid simulations: (a)–(d) As in Figs. 13i–l and (e)–(h) as in Figs. 14i–l.

Alternately, if the nested grid was shifted westward so that the Big Island of Hawaii no longer lies within the nest (Figs. 18e,j), there is no identifiable vortex shedding and the solution is similar to the c120 single-grid simulation (Figs. 18c,h). In this case, there is no visible noise in the vorticity field that might be attributed to the boundary of the nest.

e. Timing

Grid nesting would be worthless if it did not allow substantial time savings compared to a uniformly high-resolution simulation. However, the amount of message passing involved in two-way updating on parallel machines is sufficiently large that some modelers find two-way nesting prohibitively expensive (C. F. Mass 2010, personal communication). To test the performance of our grid nesting methodology, we have performed a series of Jablonowski–Williamson tests to determine the time a nested simulation takes compared to a uniform-resolution simulation with the same resolution globally as does the nested-grid simulation on its nest. Five identical 10-day simulations were performed in which no disk I/O was done to evaluate the speed of the dynamical core; otherwise the simulations were identical to those in section 3b. These simulations were performed on the Gaea supercomputer (http://www.ncrc.gov), a Cray XT6 system with 2576 12-core 2.1 GHz 64-bit AMD Opteron processors.

All of the nested simulations shown in Fig. 19 take longer to execute than a simulation of just the coarse grid using a similar number of processors. However, all of the nested-grid simulations also run faster than a single-grid simulation with the same resolution globally as on the nested grid; a uniform-resolution c180 simulation takes 1000 s with 216 processors, which is more than 4 times longer than even the slowest c90 nested-grid simulations, and 15 times longer than the fastest. A c540 simulation using 600 processors (not shown) took 8000 s to complete a 10-day integration, which is 3 times slower than the slowest c180 nested-grid simulation and 10 times slower than the fastest.

How much more expensive is running a nested grid than just its parent coarse grid? Serial nesting increases the execution time by anywhere from 60% to nearly doubling it compared to the time for just a single grid. However, using concurrent nesting, in which the nested grid receives its own set of processors, has the potential to greatly speed up nested-grid simulations, often by only adding a relatively small number of processors. Most notably, a two-way c180 concurrent-nested simulation assigning 96 processors to the coarse grid and 36 to the nested grid—for a total of 132 processors—executes in less than 10% more time than did a single c180 grid alone with 96 processors. Care must be taken to ensure that enough processes are assigned to the nested grid: for example, a c60 simulation with 24 processors assigned to the coarse grid and only 4 to the nested is actually slower than a serially nested simulation, although this problem is resolved by assigning 9 processors to the nested grid. One-way nested concurrent simulations are faster than are the equivalent two-way nested simulations, but typically by less than 10%.

While some consideration of the number of processors to be allocated to a nested grid is necessary—similar to that given to apportioning processors between the components of a coupled model—our results suggest

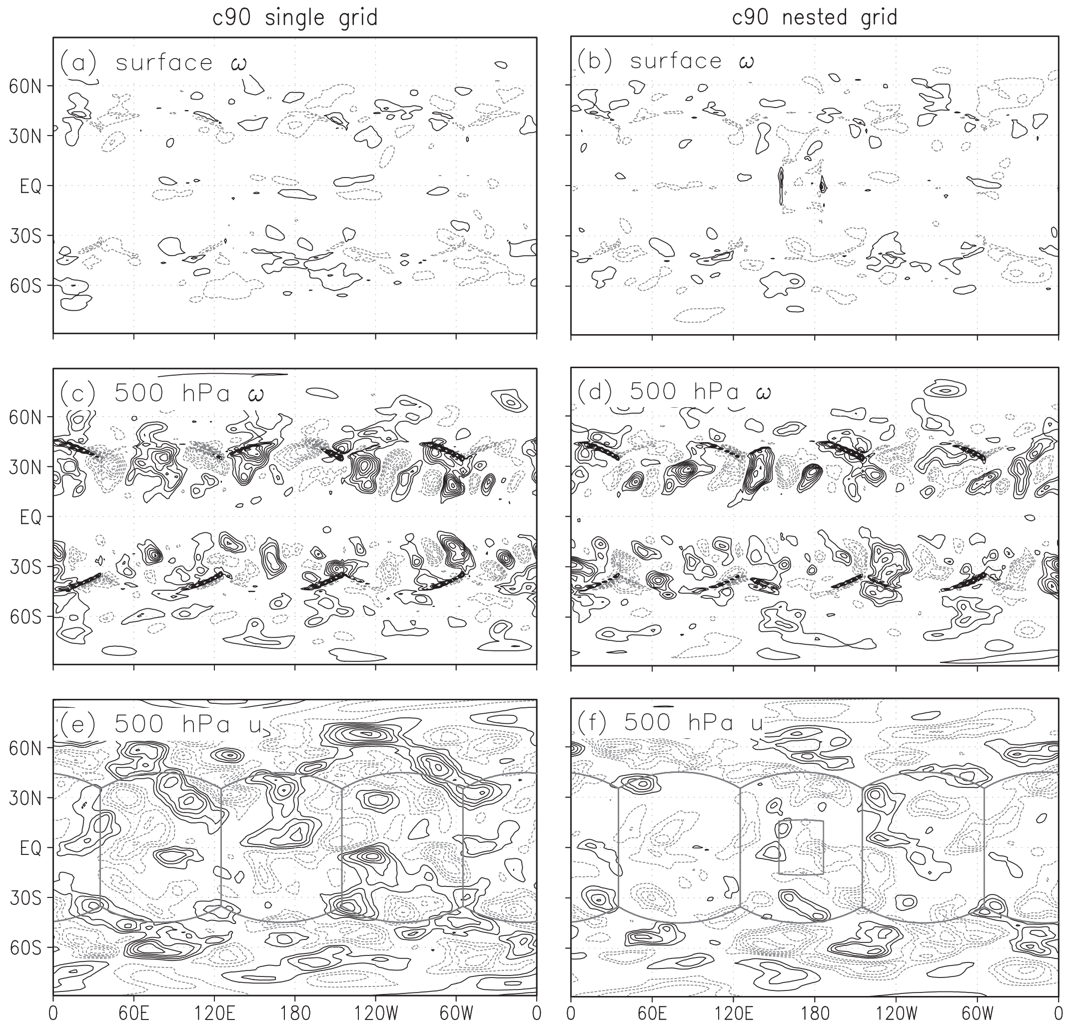

FIG. 17. As in Fig. 15, but for c90 simulations.

that a little such effort can yield a substantial improvement in computational efficiency in environments with large numbers of available processors.

4. Summary

Regional models have many disadvantages for climate simulation and for weather prediction on time scales of more than a few days, because unlike global models they require the specification of boundary conditions taken from a model that nearly always has different dynamics and numerics. Here, we present a two-way global-to-regional nested version of the FV core allowing for better resolution over a limited area using the same model equations and discretization throughout. Our nested-grid boundary conditions and nested-to-coarse two-way update are simple: the boundary conditions are simply linearly interpolated coarse-grid data, and two-way updating is simply a vorticity-conserving average to corresponding coarse-grid cells of all variables except mass, allowing us to easily achieve mass conservation on the coarse grid. We also use a ''concurrent'' nesting strategy, allowing both grids to run simultaneously using time-extrapolated boundary conditions on the nested grid. We have shown that concurrent nesting can greatly increase the efficiency of the nested model on massively-parallel systems compared to the more common ''serial'' nesting technique, with only minor increases (or even minor decreases) in the error norms.

Despite the simplicity of our nesting methodology, we find that the degradation of large-scale balanced flows, sensitive to inhomogeneities in grid structure, is limited to increases of at most a factor of 2 in global error norms when a nested grid is introduced into a uniform-resolution coarse-grid simulation. This is true for either of a pair of shallow-water test cases and in the three-dimensional

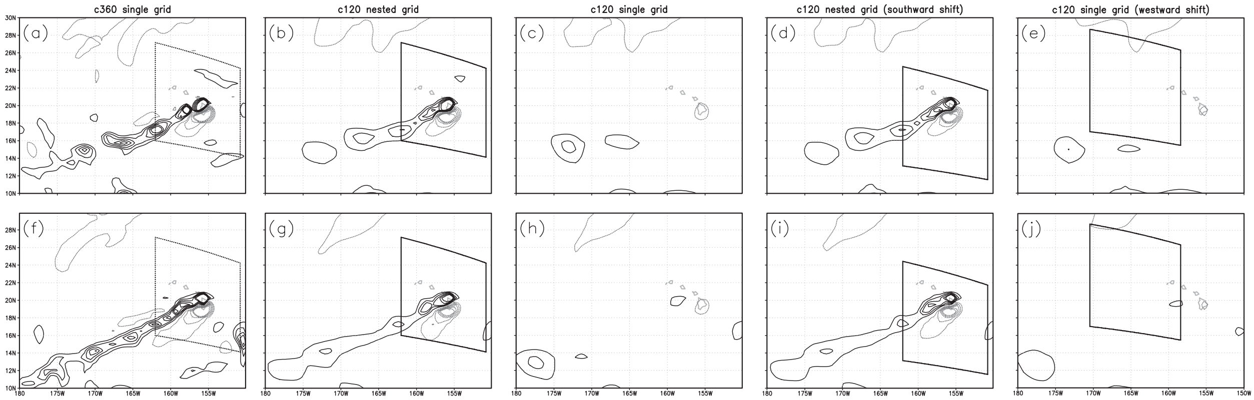

FIG. 18. Surface vorticity (contour interval 10^{-5} s^{-1}, negative values in gray, values above 5×10^{-5} s^{-1} not plotted) simulations initialized at 0000 UTC 1 Aug 2010. (a)–(e) $t = 72$ h and (f)–(j) $t = 96$ h. Hawaii is at middle right in each panel. The dotted line in (a) and (f) shows where the nest would be in the nested-grid c120 simulation.

Jablonowski–Williamson baroclinic instability test case. Furthermore, our nested-grid simulations do not lose the convergence properties of the single-grid simulations. In a Held–Suarez climate simulation, grid artifacts in the vertical velocity field at the boundary of a nested grid were comparable to those at the edges of the cubed-sphere global grid; these artifacts decreased as the resolution increased from c48 to c90, and in other model fields were imperceptible. Differences in the zonal means and eddy statistics between single- and nested-grid simulations were small compared to the magnitudes of the means themselves.

In the Jablonowski–Williamson test case, structures in a mature low were more detailed in a nested-grid simulation, without the nest disrupting the baroclinic wave train, although the nested-grid solution's low was not as well developed as that in a uniform high-resolution simulation. Also, while the low was passing through the nested-grid error norms in the nested-grid region were at most 20% larger, and at some times modestly smaller, than the corresponding single-grid simulation. However, in this test case the nested grid did not improve the solution beyond the bounds of the nest. A different test case, initialized with NCEP analyses and USGS topography, showed that a c120 simulation that could not reproduce Hawaii lee-vortex shedding seen in a c360 simulation could do so when a nested grid was introduced. The lee vortices resolved by the nested grid were also observed to propagate out of the nested region and downstream into the coarse grid.

Nesting so far has been implemented and tested in idealized, dry simulations; work is planned to extend the nesting to simulations with full physics and to enable moving grids that can track a propagating disturbance, such as a tropical storm or pollutant plume. Also planned is two-way updating that only transmits the part of the nested grid that will affect the coarse grid outside of

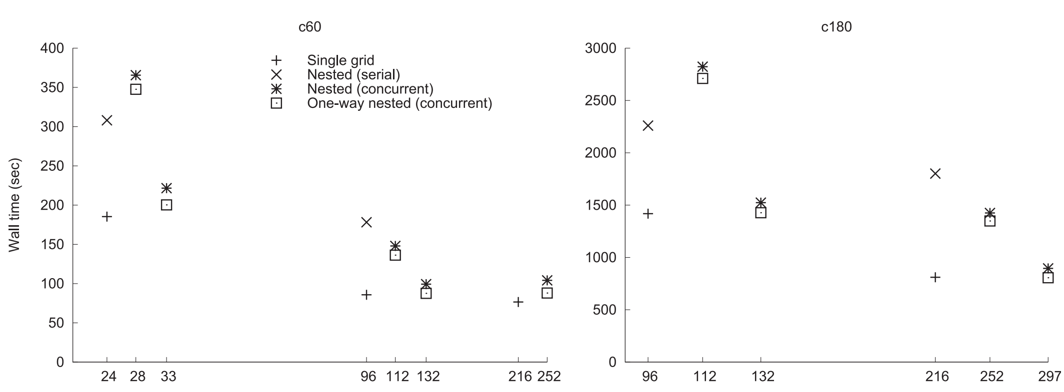

FIG. 19. Averaged elapsed wall-clock time for five identical Jablonowski–Williamson simulations for different resolutions and nesting strategies. Concurrent simulations using 28 or 33 processors assign 24 to the coarse grid and the remainder to the nested grid; those using 112 or 132 processors assign 96 to the coarse grid; and those using 252 or 297 processors assign 216 to the coarse grid.

the nest, greatly decreasing the amount of data to pass between processors and ideally speeding up two-way simulations. The nesting described in this paper is being implemented in GFDL High-Resolution Atmospheric Model (HiRAM; Zhao et al. 2009; Chen and Lin 2011).

Acknowledgments. LMH was partially supported by NOAA's Hurricane Forecast Improvement Project. Concurrent nesting was originally suggested by V. Balaji. Comments from Bruce Wyman, Alistair Adcroft, Todd Ringler, and three anonymous referees were greatly appreciated.

APPENDIX

Concurrent Grid Nesting Algorithm

The following is a pseudocode algorithm describing the concurrent grid nesting introduced in section 2b.

Initialization

If a nested grid, compute interpolation weights for each boundary (halo) point:

$$w^1_{i,j} = |y_{i,j} - Y_{I,J+1}||x_{i,j} - X_{I+1,J}|$$
$$w^2_{i,j} = |y_{i,j} - Y_{I,J}||x_{i,j} - X_{I+1,J}|$$

$$w^3_{i,j} = |y_{i,j} - Y_{I,J}||x_{i,j} - X_{I,J}|$$
$$w^4_{i,j} = |y_{i,j} - Y_{I,J+1}||x_{i,j} - X_{I,J}|,$$

where i, j are nested-grid indices; $I = I_0 + \lfloor (i-1)/r \rfloor - 1$ and $J = J_0 + \lfloor (j-1)/r \rfloor - 1$ are the coarse-grid indices; r is the nested-grid refinement ratio; (I_0, J_0) is the index of the coarse-grid cell whose lower-left corner coincides with the lower-left corner of the nested grid; $(x, y)_{i,j}$ and $(X, Y)_{I,J}$ are the gnomonic coordinates of a nested- and coarse-grid cell centroid, respectively; $|\cdot|$ is the great-circle distance between two points; and $\lfloor \cdot \rfloor$ is the integer floor function. All indices are one based. (For face-averaged variables, a different set of weights are computed, in which face centroids are used in place of cell centroids.)

For each large time step, starting at time t and integrating to time $t + \Delta\tau$:

If a nested grid, receive BC data $\Psi^t_{I,J}$ from parent
Send data $\phi^t_{i,j}$ to nested grids, if any
Perform linear interpolation from coarse grid to nested grid BC points:

$$\phi^t_{i,j} = w^1_{i,j}\Psi^t_{I,J} + w^2_{i,j}\Psi^t_{I,J+1} + w^3_{i,j}\Psi^t_{I+1,J+1} + w^4_{i,j}\Psi^t_{I+1,J}$$

do small time steps $n = 1, N$

If a nested grid, set BCs to time-extrapolated values of previously space-interpolated coarse-grid data: if (i, j) is in the nested-grid outer halo, then

$$\phi^{t+n\delta t}_{i,j} = \left(1 + \frac{n}{N}\right)\phi^t_{i,j} - \frac{n}{N}\phi^{t-\Delta\tau}_{i,j},$$

If this is the first time step of a simulation, simply use $\phi^{t+n\delta t}_{i,j} = \phi^t_{i,j}$.
Advance FV core solution by $\delta t = \Delta t/N$ to get $\phi^{t+n\delta t}_{i,j}$.

end do
Perform vertical remapping, if a 3D simulation.
Perform physics or Held–Suarez forcing, if enabled.
If this grid is the parent of a two-way nested grid

Receive solution $\varphi^{t+\Delta t}_{\mu,\nu}$ from nest.
If ϕ is a cell-average value, set

$$\phi^{t+\Delta\tau}_{i,j} = \frac{1}{r^2}\sum_{n=1}^{r}\sum_{m=1}^{r}\varphi^{t+\Delta\tau}_{\mu_0+m,\nu_0+n},$$

where (μ_0, ν_0) is the index of the nested-grid cell sharing a lower-left corner with the parent-grid cell (i, j).
If ϕ is a face-average value,
If the face lies in the x-direction, set

$$\phi^{t+\Delta\tau}_{i,j} = \frac{1}{r}\sum_{m=1}^{r}\varphi^{t+\Delta\tau}_{\mu_0+m,\nu_0},$$

Else if the face lies in the y-direction, set

$$\phi^{t+\Delta\tau}_{i,j} = \frac{1}{r}\sum_{n=1}^{r}\varphi^{t+\Delta\tau}_{\mu_0,\nu_0+n},$$

end if
If this is a two-way nested grid, send solution $\phi^{t+\Delta\tau}_{i,j}$ to parent.
End large time step.

REFERENCES

Atlas, R., and Coauthors, 2005: Hurricane forecasting with the high-resolution NASA finite volume general circulation model. *Geophys. Res. Lett.*, **32,** L03807, doi:10.1029/2004GL021513.

Berger, M., and P. Colella, 1989: Local adaptive mesh refinement for shock hydrodynamics. *J. Comput. Phys.*, **82,** 64–84.

Bernard, P.-E., J.-F. Remacle, R. Comblen, V. Legat, and K. Hillewaert, 2009: High-order discontinuous Galerkin schemes on general 2D manifolds applied to the shallow water equations. *J. Comput. Phys.*, **228** (17), 6514–6535, doi:10.1016/j.jcp.2009.05.046.

Bey, I., and Coauthors, 2001: Global modeling of tropospheric chemistry with assimilated meteorology: Model description and evaluation. *J. Geophys. Res.*, **106** (D19), 23 073–23 095.

Chen, J.-H., and S.-J. Lin, 2011: The remarkable predictability of inter-annual variability of Atlantic hurricanes during the past decade. *Geophys. Res. Lett.,* **38,** L11804, doi:10.1029/2011GL047629.

Chen, W., Z. Jiang, L. Li, and P. Yiou, 2011: Simulation of regional climate change under the IPCC A2 scenario in southeast China. *Climate Dyn.,* **36,** 491–507, doi:10.1007/s00382-010-0910-3.

Colella, P., and P. R. Woodward, 1984: The piecewise parabolic method (PPM) for gas-dynamical simulations. *J. Comput. Phys.,* **54,** 174–201.

Courtier, P., and J. Geleyn, 1988: A global numerical weather prediction model with variable resolution: Application to the shallow-water equations. *Quart. J. Roy. Meteor. Soc.,* **114,** 1321–1346.

Delworth, T., and Coauthors, 2006: GFDL's CM2 global coupled climate models. Part I: Formulation and simulation characteristics. *J. Climate,* **19,** 643–674.

Donner, L., and Coauthors, 2011: The dynamical core, physical parameterizations, and basic simulation characteristics of the atmospheric component AM3 of the GFDL global coupled model CM3. *J. Climate,* **24,** 3484–3519.

Dudhia, J., and J. Bresch, 2002: A global version of the PSU–NCAR mesoscale model. *Mon. Wea. Rev.,* **130,** 2989–3007.

Fox-Rabinovitz, M., J. Côté, B. Dugas, M. Déqué, and J. McGregor, 2006: Variable resolution general circulation models: Stretched-grid model intercomparison project (SGMIP). *J. Geophys. Res.,* **111,** D16104, doi:10.1029/2005JD006520.

Giorgi, F., and L. Mearns, 1999: Regional climate modeling revisited: An introduction to the special issue. *J. Geophys. Res.,* **104** (D6), 6335–6352.

Harris, L., and D. Durran, 2010: An idealized comparison of one-way and two-way grid nesting. *Mon. Wea. Rev.,* **138,** 2174–2187.

——, P. Lauritzen, and R. Mittal, 2011: A flux-form version of the conservative semi-Lagrangian multi-tracer transport scheme (CSLAM) on the cubed sphere grid. *J. Comput. Phys.,* **230** (4), 1215–1237.

Held, I. M., and M. J. Suarez, 1994: A proposal for the intercomparison of the dynamical cores of atmospheric general circulation models. *Bull. Amer. Meteor. Soc.,* **75,** 1825–1830.

Hollingsworth, A., P. Kållberg, V. Renner, and D. Burridge, 1983: An internal symmetric computational instability. *Quart. J. Roy. Meteor. Soc.,* **109,** 417–428.

Inatsu, M., and M. Kimoto, 2009: A scale interaction study on East Asian cyclogenesis using a general circulation model coupled with an interactively nested regional model. *Mon. Wea. Rev.,* **137,** 2851–2868.

Jablonowski, C., and D. L. Williamson, 2006: A baroclinic instability test case for atmospheric model dynamical cores. *Quart. J. Roy. Meteor. Soc.,* **132,** 2943–2975.

Krol, M., and Coauthors, 2005: The two-way nested global chemistry-transport zoom model TM5: Algorithm and applications. *Atmos. Chem. Phys.,* **5,** 417–432.

Kurihara, Y., G. Tripoli, and M. Bender, 1979: Design of a movable nested-mesh primitive equation model. *Mon. Wea. Rev.,* **107,** 239–249.

Lauritzen, P. H., 2007: A stability analysis of finite-volume advection schemes permitting long time steps. *Mon. Wea. Rev.,* **135,** 2658–2673.

Lee, J., and A. MacDonald, 2009: A finite-volume icosahedral shallow-water model on a local coordinate. *Mon. Wea. Rev.,* **137,** 1422–1437.

Li, X., D. Chen, X. Peng, K. Takahashi, and F. Xiao, 2008: A multimoment finite-volume shallow-water model on the Yin–Yang overset spherical grid. *Mon. Wea. Rev.,* **136,** 3066–3086.

Lin, S.-J., 1997: A finite-volume integration method for computing pressure gradient force in general vertical coordinates. *Quart. J. Roy. Meteor. Soc.,* **123,** 1749–1762.

——, 2004: A ''vertically Lagrangian'' finite-volume dynamical core for global models. *Mon. Wea. Rev.,* **132,** 2293–2307.

——, and R. Rood, 1996: Multidimensional flux-form semi-Lagrangian transport schemes. *Mon. Wea. Rev.,* **124,** 2046–2070.

——, and ——, 1997: An explicit flux-form semi-Lagrangian shallow-water model on the sphere. *Quart. J. Roy. Meteor. Soc.,* **123,** 2477–2498.

——, R. Atlas, and K. Yeh, 2004: Global weather prediction and high-end computing at NASA. *Comput. Sci. Eng.,* **6** (1), 29–35.

Long, D., and J. Thuburn, 2011: Numerical wave propagation on non-uniform one-dimensional staggered grids. *J. Comput. Phys.,* **230** (7), 2643–2659.

Lorenz, P., and D. Jacob, 2005: Influence of regional scale information on the global circulation: A two-way nesting climate simulation. *Geophys. Res. Lett.,* **32,** L18706, doi:10.1029/2005GL023351.

Oliger, J., and A. Sundström, 1978: Theoretical and practical aspects of some initial boundary value problems in fluid dynamics. *SIAM J. Appl. Math.,* **35** (3), 419–446, doi:10.1137/0135035.

Putman, W. M., 2007: Development of the finite-volume dynamical core on the cubed-sphere. Ph.D. thesis, The Florida State University, 101 pp.

——, and S.-J. Lin, 2007: Finite-volume transport on various cubed-sphere grids. *J. Comput. Phys.,* **227,** 55–78.

Richardson, M., A. Toigo, and C. Newman, 2007: PlanetWRF: A general purpose, local to global numerical model for planetary atmospheric and climate dynamics. *J. Geophys. Res.,* **112,** E09001, doi:10.1029/2006JE002825.

Ringler, T., D. Jacobsen, M. Gunzburger, L. Ju, M. Duda, and W. Skamarock, 2011: Exploring a multi-resolution modeling approach within the shallow-water equations. *Mon. Wea. Rev.,* **139,** 3348–3368.

Rossmanith, J. A., 2006: A wave propagation method for hyperbolic systems on the sphere. *J. Comput. Phys.,* **213** (2), 629–658, doi:10.1016/j.jcp.2005.08.027.

Smith, R., and V. Grubišić, 1993: Aerial observations of Hawaii's wake. *J. Atmos. Sci.,* **50,** 3728–3750.

St-Cyr, A., C. Jablonowski, J. Dennis, H. Tufo, and S. Thomas, 2008: A comparison of two shallow-water models with nonconforming adaptive grids. *Mon. Wea. Rev.,* **136,** 1898–1922.

Suresh, A., and H. Huynh, 1997: Accurate monotonicity-preserving schemes with Runge–Kutta time stepping. *J. Comput. Phys.,* **136,** 83–99.

Temam, R., and J. Tribbia, 2003: Open boundary conditions for the primitive and Boussinesq equations. *J. Atmos. Sci.,* **60,** 2647–2660.

Thuburn, J., and Y. Li, 2000: Numerical simulations of Rossby-Haurwitz waves. *Tellus,* **52A,** 181–189.

Tribbia, J., and R. Temam, 2011: Waves, hyperbolicity and characteristics. *Numerical Techniques for Global Atmospheric Models,* P. H. Lauritzen et al., Eds., Springer, 29–42.

Ullrich, P., C. Jablonowski, and B. Van Leer, 2010: High-order finite-volume methods for the shallow-water equations on the sphere. *J. Comput. Phys.,* **229** (17), 6104–6134.

Vichnevetsky, R., 1987: Wave propagation and reflection in irregular grids for hyperbolic equations. *Appl. Numer. Math.,* **3,** 133–166.

Warner, T., R. Peterson, and R. Treadon, 1997: A tutorial on lateral boundary conditions as a basic and potentially serious limitation to regional numerical weather prediction. *Bull. Amer. Meteor. Soc.,* **78,** 2599–2617.

Weller, H., H. Weller, and A. Fournier, 2009: Voronoi, Delaunay, and block-structured mesh refinement for solution of the shallow-water equations on the sphere. *Mon. Wea. Rev.,* **137,** 4208–4224.

Williamson, D., J. Drake, J. Hack, R. Jakob, and P. Swarztrauber, 1992: A standard test set for numerical approximations to the shallow water equations in spherical geometry. *J. Comput. Phys.,* **102,** 211–224.

Zhang, D.-L., H.-R. Chang, N. L. Seaman, T. Warner, and J. Fritsch, 1986: A two-way interactive nesting procedure with variable terrain resolution. *Mon. Wea. Rev.,* **114,** 1330–1339.

Zhao, M., I. M. Held, S.-J. Lin, and G. A. Vecchi, 2009: Simulations of global hurricane climatology, interannual variability, and response to global warming using a 50-km resolution GCM. *J. Climate,* **22,** 6653–6678.